Cardiac motion estimation using covariant derivatives and Helmholtz decomposition

EINDHOVEN UNIVERSITY OF TECHNOLOGY
Department of Mathematics and Computer Science

CASA-Report 10-31
June 2010

Cardiac motion estimation using covariant derivatives and Helmholtz decomposition

by

R. Duits, A. Becciu, B.J. Janssen, L.M.J. Florack,
H. van Assen, B. ter Haar Romeny

Centre for Analysis, Scientific computing and Applications
Department of Mathematics and Computer Science
Eindhoven University of Technology
P.O. Box 513
5600 MB Eindhoven, The Netherlands
ISSN: 0926-4507

Cardiac Motion Estimation using Covariant Derivatives and Helmholtz Decomposition

Remco Duits[1,2], Alessandro Becciu[2], Bart Janssen[1],
Luc Florack[1,2], Hans van Assen[2] and Bart ter Haar Romeny[2]

Department of Mathematics and Computer Science[1] and
Department of Biomedical Engineering[2], Eindhoven University of Technology (TU/e).

May 26, 2010.

Abstract

The investigation and quantification of cardiac movement is important for assessment of cardiac abnormalities and treatment effectiveness. Therefore we consider new aperture problem-free methods to track cardiac motion from 2-dimensional MR tagged images and corresponding sine-phase images. Tracking is achieved by following the movement of scale-space maxima, yielding a sparse set of linear features of the unknown optic flow vector field. Interpolation/reconstruction of the velocity field is then carried out by minimizing an energy functional which is a Sobolev-norm expressed in covariant derivatives (rather than standard derivatives). These covariant derivatives are used to express prior knowledge about the velocity field in the variational framework employed. They are defined on a fiber bundle where sections coincide with vector fields. Furthermore, the optic flow vector field is decomposed in a divergence free and a rotation free part, using our multi-scale Helmholtz decomposition algorithm that combines diffusion and Helmholtz decomposition in a single non-singular analytic kernel operator. Finally, we combine this multi-scale Helmholtz decomposition with vector field reconstruction (based on covariant derivatives) in a single algorithm and present some experiments of cardiac motion estimation. Further experiments on phantom data with ground truth show that both the inclusion of covariant derivatives and the inclusion of the multi-scale Helmholtz decomposition improves the optic flow reconstruction.

1 Introduction

In cardiology literature [10] it has been noted that variation in thickness of the cardiac wall may provide quantitative indication of the health of the cardiac muscle. Cardiac motion extraction is therefore an important area of research, since monitoring and quantification of irregular cardiac wall deformation may help in early diagnosis of cardiac abnormalities such as ischemia, area of tissue resulting from obstruction of blood circulation, as well as in providing information about the effectiveness of treatment. In order to characterize the contracting behavior of the cardiac muscle, non-invasive acquisition techniques such as MR tagging can been applied. This methodology allows to superimpose artificial brightness patterns on the image, which deform according to the cardiac muscle and aid to retrieve motion within the heart walls.

The problem of extracting motion in image sequences is of primary interest for the computer vision and image analysis community. Optic flow measures apparent motion of moving patterns in image sequences, providing information about spatial displacements of objects in consecutive frames. At the beginning of the eighties Horn and Schunck introduced a mathematical formulation of optic flow assuming that intensities associated to image objects did not change along the sequence, [25]. This formulation has been referred as the Optic Flow Constraint Equation (OFCE):

$$f_x u + f_y v + f_t = 0 \tag{1.1}$$

where $(x, y, t) \to f(x, y, t) : \mathbb{R}^2 \times \mathbb{R}^+ \to \mathbb{R}$ is an image sequence, f_x, f_y, f_t are the spatial and temporal derivatives; $\mathbf{v}(\cdot, t)$ is a vector field on $\mathbb{R}^2$ given by $\mathbf{v}(x, y, t) = (u(x, y, t), v(x, y, t))^T$, where u and v are unknown and x, y and t are the spatial and temporal coordinates respectively. Since scalar-valued functions

u and v are unknown, equation (1.1) does not generate unique solution, providing the so-called "aperture problem" and therefore Horn and Schunck added a homogeneous smoothness constraint based on gradient magnitude to a data term, equation (1.1), and minimized the energy functional using a variational approach [25]. A similar scheme has been employed in more recent and sophisticated techniques by Bruhn et al. [6] and Zimmer et al.[52], who used an anisotropic smoothness term and carried out tests on the Yosemite sequence and Middlebury benchmark outperforming the results of most of the current optic flow methods. A multi-scale extension of equation (1.1) has been investigated by Florack et al.[14] and an application to cardiac tagged MR images has been further explored in [38, 45, 2, 13]. Extraction of object displacements has been studied also by means of feature tracking. Thyrion [46] has investigated a technique, where the brightness is preserved and the features are driven to the most likely positions by forces. Janssen et al. and Van Dorst et al. [8, 29] propose multi-scale feature based optic flow methods, where the reconstruction of the dense flow field is obtained from a sparse set of velocities associated to multi-scale anchor points.

These methods, however, are rather general and do not take into account physical properties of the velocity field generated by rotation and compressibility of the cardiac tissue. Local rotation and contraction of the cardiac muscle can be calculated by investigating the divergence free and rotation free parts of the well-known Helmholtz decomposition [23, 1]. Exploring this decomposition may play a fundamental role in the clinical diagnosis procedure, since it reveals abnormalities in tissue deformation, such as stiffness. Therefore, for applications such as cardiac motion extraction, blood flow calculation and fluid motion analysis information of such properties may be more suitable and lead to an more accurate velocity field estimation in comparison to general approaches. Examples of such optic flow methods have been provided by [20, 7, 32].

In this work we extract 2-dimensional cardiac wall motion by employing an optic flow method based on features points such as maxima, minima and saddles. The dense flow field has been reconstructed by employing variational methods; in the smoothness term we include information obtained by our multi-scale Helmholtz decomposition and we describe the regularization components in terms of covariant derivatives biased by a gauge field. Advantages of this approach are significant:

(i) We do not suffer from the aperture problem.

(ii) The features are not depending on constant brightness, since critical points such as maxima will retain their characterization even after presence of fading in the image. Therefore, the algorithm can be robustly applied on image sequences (like tagged MR images) where the intensity constancy is not preserved.

(iii) The proposed technique takes into account physical properties of contractibility and rotation of the heart muscle by means of a multi-scale Helmholtz decomposition.

(iv) The algorithm takes the advantages provided by a multi-scale approach:

- A scale selection scheme for the feature points will be further discussed in the paper.
- In our multi-scale we *analytically pre-compute* the concatenation of linear diffusion operator combined with Helmholtz decomposition in a single non-singular kernel operator in order to avoid grid artefacts. Here we do not use more elaborate, discrete multi-scale Helmholtz decompositions, cf. [47], which act by means of nonlinear diffusions on the potentials, since in our linear reconstruction algorithm we need to keep track of a consistent and basic notion of scale, avoid sensitive nonlinear diffusion parameters, diffuse the field itself and finally we need efficient computation.

(v) Finally we investigate a new regularization component described in terms of covariant derivatives in a fiber bundle, where sections coincide with the graphs of functions. The regularization term includes information from a so-called gauge field and allows a better flow field reconstruction with respect to the one provided by similar techniques, which use standard derivatives [5] instead. For a different optic flow approach where pre-knowledge in the regularization term is included we refer to Nir et al. [39].

(vi) Both the computation of the gauge field and the subsequent reconstruction framework (with given gauge field) are stable linear operators (due to the coercivity of the covariant Laplacian).

In the experiment we assess the algorithm performance with a phantom from which the ground truth was known and tests have been carried out with real data obtained from a patient and a healthy volunteer. Quantitative and qualitative analysis shows reliability of the extracted motion field.

Outline of algorithm and article

An overview of the proposed algorithm is provided in figure 1 and every step is described as follows. In section 2 we illustrate preprocessing steps followed to convert raw data in phase images. In section 3, we define the scale space framework, use the winding number as a tool to extract critical points in scale space and a technique to refine the position of retrieved feature points up to sub-pixel location. Section 4 describes a methodology used to calculate velocity features including a scale selection scheme. Section 5 is dedicated to the multi-scale Helmholtz decomposition of vector fields, where we analytically compute the effective kernel operator that arises by concatenation of the (commuting) linear diffusion operator and Helmholtz-decomposition operator.

In sections 6, 7 we introduce the concept of covariant derivatives. Subsequently, in Section 8 we consider dense motion field reconstruction by energy minimization where the data-term is obtained by our methodology explained in Section 3 and Section 4 and where the smoothness term takes care of Tikhonov regularization expressed in the covariant derivatives of Section 7. Here we derive the corresponding Euler-Lagrange equations and prove that the explicitly derived solutions are stable, both in the continuous and the discrete setting (using a B-spline basis). Then in Section 9 we put everything together and include the multi-scale Helmholtz decomposition in the dense motion field reconstruction. Here we distinguish between two options, a pragmatic one which consists of two separate reconstruction algorithms for divergence and rotation free part and a theoretic one where we merge everything into a single energy minimization yielding a related but more difficult Euler-Lagrange system. Finally in section 10 and 11 we present and discuss the outcomes of the experiments we have carried out.

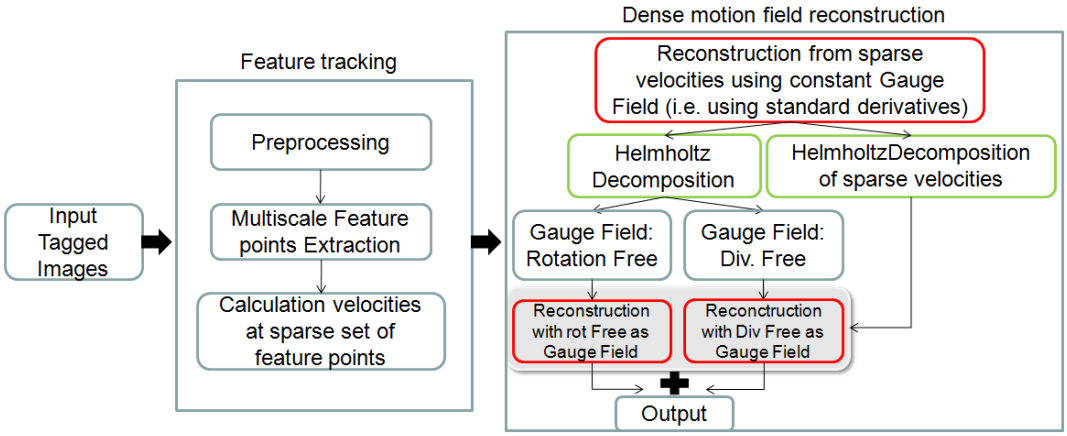

Figure 1: Overview of the algorithm. Input tagged images and first preprocessing steps are discussed in section 2. The feature tracking procedure is described in Sections 3 and 4. Sections 6 and 7 explain the concept of covariant derivatives and in Section 5 we present our multi-scale Helmholtz decomposition algorithm. The box on the right shows how these two techniques are applied in the dense motion field reconstruction which we present in Sections 8 and 9.

2 Image data set and sine-phase images

Tagging is a noninvasive technique based on local perturbing the magnetization of the cardiac tissue via radio frequency impulses. MR Tags are artificial patterns, represented as dark stripes and superimposed on the MR images with the aim to improve the visualization of the deforming tissue[51]. An example of a tagged

heart image is displayed in figure 2, column 1. In order to increase the number of tags in the image, Axel and Dougherty [3] spatially modulated the degree of magnetization in the cardiac tissue, whereas Osman et al. [40] proposed the so-called harmonic phase (HARP) method, which converts MR images in phase images. In our experiments we apply a similar technique and we extract phase images by means of Gabor filters [16] (figure 2, column 2). Such images allow to extract feature points such as maxima minima and saddles with high accuracy. The calculated phase images (in the experiment we employ the sine function for smoothing purposes) have been combined in order to create a chessboard-like grid from which critical points have been retrieved. Throughout this article we will apply our methods to phase images as can be seen in Figure 2, column 3.

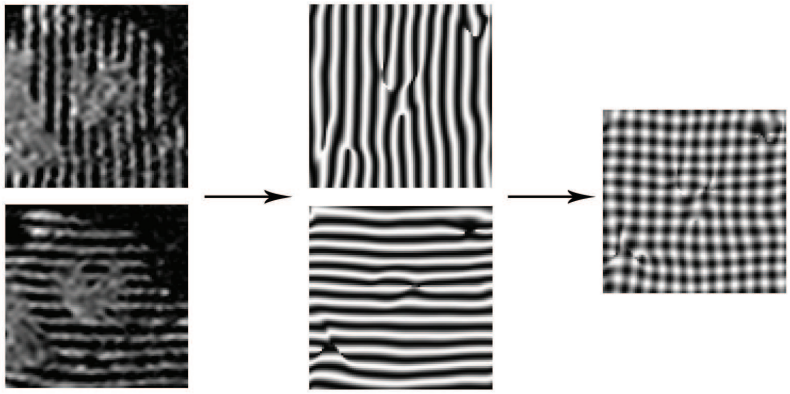

Figure 2: Column 1: Short axis view of patient left ventricle. Column 2. Sine-phase images. Column 3. Sum of sine-phase images. This sum of sine phase images serves as input in our algorithms and will be denoted by $f(\mathbf{x}, t)$ where $\mathbf{x} = (x, y) \in \mathbb{R}^2$ denotes position and $t > 0$ denotes time.

3 Extraction of critical points in scale space

Our visual system observes (objects in) an image simultaneously at multiple scales. The Gaussian scale space representation $I : \mathbb{R}^2 \times \mathbb{R}^+$ of a 2-dimensional *static* image $\mathbf{x} \mapsto f(\mathbf{x}) \in \mathbb{L}_2(\mathbb{R}^2)$ is defined by the spatial convolution with a Gaussian kernel

$$I(\mathbf{x}, s) = (f * \phi_s)(\mathbf{x}) \ , \text{ with } \phi_s(\mathbf{x}) = \frac{1}{4\pi s} \exp(-\frac{\|\mathbf{x}\|^2}{4s}) \ , s > 0, \tag{3.2}$$

where $\mathbf{x} = (x, y) \in \mathbb{R}^2$ and where $s > 0$ represents the scale of observation [26, 49, 34, 35, 31, 21, 12]. Recall that (3.2) is the solution of a diffusion system on the upper half space $s > 0$, so $\frac{\partial}{\partial s} I = \Delta I$ and $\lim_{s \downarrow 0} I(\cdot, s) = f$ $\lim_{s \to \infty} I(\cdot, s) = 0$ where both limits are taken in $\mathbb{L}_2$-sense. This procedure naturally extends to a multiple scale representation of a *dynamic* image $(x, y, t) \mapsto f(x, y, t)$:

$$I(x, y, s, t) := (G_s * f(\cdot, \cdot, t))(x, y), \qquad t, s > 0, \mathbf{x} = (x, y) \in \mathbb{R}^2,$$

A convenient tool to extract and classify critical points at different scales is represented by the so-called topological number [44]. The topological number characterizes the local structure of a function by exploring the neighborhood of a certain point. For 2-dimensional functions topological number is denoted as *winding number* and represents the integrated change of the angle of the gradient when traversing a closed curve in a plane. The winding number is always an integer multiple of 2π and its value classifies intrinsically the extracted critical point. The winding number is zero for regular points, it is $+2\pi$ for extrema, and -2π for saddle points.

3.1 Critical point position refinement

Due to signal discretization, the retrieved critical point location (for example computed by means of the winding number) does not correspond most likely to the real extremum or saddle point position (figure 3). This problem can be solved by describing a fixed time frame image $I(\cdot, s, t)$, with $s, t > 0$ fixed, in terms of Taylor series such that

$$\nabla I(\mathbf{x}_a, s, t) = \begin{bmatrix} I_x(\mathbf{x}_e, s, t) + (x_a - x_e) I_{xx}(\mathbf{x}_e, s, t) + (y_a - y_e) I_{xy}(\mathbf{x}_e, s, t) \\ I_y(\mathbf{x}_e, s, t) + (x_a - x_e) I_{yx}(\mathbf{x}_e, s, t) + (y_a - y_e) I_{yy}(\mathbf{x}_e, s, t) \end{bmatrix} \tag{3.3}$$

where $\mathbf{x}_a = (x_a, y_a)$ and $\mathbf{x}_e = (x_e, y_e)$ represent the true and the estimated critical point location respectively. At critical point positions the image gradient vanishes, therefore the l.h.s. of equation (3.3) vanishes, hence

$$\mathbf{x}_a = \begin{bmatrix} x_a \\ y_a \end{bmatrix} = \begin{bmatrix} x_e \\ y_e \end{bmatrix} - \begin{bmatrix} I_{xx}(\mathbf{x}_e, s, t) I_{xy}(\mathbf{x}_e, s, t) \\ I_{yx}(\mathbf{x}_e, s, t) I_{yy}(\mathbf{x}_e, s, t) \end{bmatrix}^{-1} \begin{bmatrix} I_x(\mathbf{x}_e, s, t) \\ I_y(\mathbf{x}_e, s, t) \end{bmatrix} \tag{3.4}$$

Equation (3.4) provides position estimation at subpixel level and can be iterated until the desired accuracy has been reached. In the remainder of this article refined critical points positions will be abbreviated as follows $\mathbf{x} = \mathbf{x}_a$.

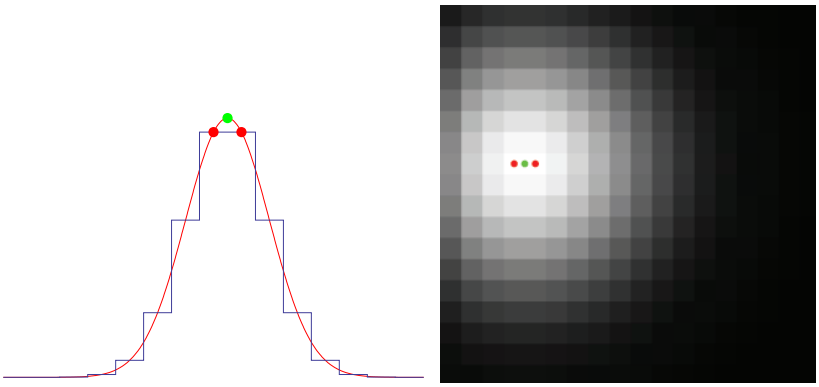

Figure 3: Critical point refinement. Left: a continuum gaussian signal in 1 dimension versus its discretized correspondent. The discrete image shows maxima at two nearby positions(points in red), which are at different locations from real maximum (point in green). Right: 2 dimensional representation of the left image. Red points are the retrieved maxima, whereas the green point is true maximum obtained after the refinement.

4 Calculation of sparse velocity features

The chessboard like pattern displayed in Figure 2 consists of stripes that move along with the moving tissue, as a property of MR tags. We are interested in tracking critical points that occur at and between the tags crossing. Critical points move along with the tissue as part of the tags and are locations where the image gradient vanishes. Fading is one of MR tag artifacts and occurs due to relaxation time T1 and T2. This property, however, does not affect the image vanishing gradient and therefore does not affect the critical point localization.

In tracking critical points over time we satisfy the equation

$$\nabla I(\mathbf{x}_s^q(t_k), s, t_k) = 0 \tag{4.5}$$

where ∇ denotes the *spatial* gradient and $I(\mathbf{x}_s^q, s, t_k)$ represents intensity at position $\mathbf{x}_s^q$, scale s and time frame t_k, where $\mathbf{x}_s^q(t) = \mathbf{x}_s^q(0) + \int_0^t \widetilde{\mathbf{v}}_q(\mathbf{x}_s^q(\tau)) d\tau$ such that $\frac{d}{dt}\mathbf{x}_s^q(t) = \widetilde{\mathbf{v}}_q(\mathbf{x}_s^q(t))$ with $\mathbf{v}(\mathbf{x}(t), t) = \widetilde{\mathbf{v}}(\mathbf{x}(t))$.

Index $k = 1...K$ corresponds to the time frame number and $q = 1...N_B$ represents the branch of a certain critical point. K and N_B denote the amount of frames and critical points respectively. Differentiating equation (4.5) with respect to time t_k and applying the chain rule for the implicit functions yields

$$\frac{d}{dt}[\nabla I(\mathbf{x}_s^q(t), s, t)]\Big|_{t=t_k} = \begin{bmatrix} I_{xx}(\mathbf{x}_s^q(t_k), s, t_k)\widetilde{u}_q(\mathbf{x}_s^q(t_k)) + I_{xy}(\mathbf{x}_s^q(t_k), s, t_k)\widetilde{v}_q(\mathbf{x}_s^q(t_k)) + I_{xt}(\mathbf{x}_s^q(t_k), s, t_k) \\ I_{yx}(\mathbf{x}_s^q(t_k), s, t_k)\widetilde{u}_q(\mathbf{x}_s^q(t_k)) + I_{yy}(\mathbf{x}_s^q(t_k), s, t_k)\widetilde{v}_q(\mathbf{x}_s^q(t_k)) + I_{yt}(\mathbf{x}_s^q(t_k), s, t_k) \end{bmatrix} = 0 \tag{4.6}$$

where $\frac{d}{dt}$ is the total time derivative. In order to extract the critical point velocities, we can rewrite equation (4.6) as:

$$\begin{bmatrix} \widetilde{u}(\mathbf{x}_s^q(t_k)) \\ \widetilde{v}(\mathbf{x}_s^q(t_k)) \end{bmatrix} = \begin{bmatrix} u(\mathbf{x}_s^q(t_k), t_k) \\ v(\mathbf{x}_s^q(t_k), t_k) \end{bmatrix} = -(HI(\cdot, \cdot, t_k)(\mathbf{x}_s^q, s))^{-1} \frac{\partial(\nabla I(\mathbf{x}_s^q, s, t_k))^T}{\partial t_k} \tag{4.7}$$

where H represents the spatial Hessian matrix of image I. The scalars $\widetilde{u}(\mathbf{x}_s^q(t_k)$ and $\widetilde{v}(\mathbf{x}_s^q(t_k)$ are the horizontal and vertical components of a velocity vector at position $\mathbf{x}_s^q$ at the time t_k at scale $s > 0$.

In the remainder of this article we will abbreviate the velocity vectors at the critical points as follows

$$\mathbf{d}_q^k := \begin{pmatrix} d_q^{k,1} \\ d_q^{k,2} \end{pmatrix} := \begin{pmatrix} \widetilde{u}(\mathbf{x}_s^q(t_k)) \\ \widetilde{v}(\mathbf{x}_s^q(t_k)) \end{pmatrix} . \tag{4.8}$$

In the subsequent section we will consider a scale selection scheme per extremal branch indexed by q and per time-frame $t > 0$.

4.1 Scale selection for features at fixed time frames

So far we assumed that velocities are retrieved at a certain scale without specifying the size of basis function (gaussian filter) applied at each critical point location. The choice of scale higher than zero may provide more robustness with respect to the noise due to smoothing related to the increase of scale, moreover, the appropriate scale at different locations of cardiac muscle may be different, since the heart presents different deformations in different regions.

In choosing the scale, we consider the strength of blobs moving in the image sequence. The stronger a blob is in scale space, the more vertical is its critical path and the higher is the scale of the corresponding annihilation point (top point). A top point $(\mathbf{x}, s)$ is a singular point in scale space where the gradient and the determinant of the spatial Hessian with respect to an image I vanish [33, 41], i.e.

$$\nabla I(\mathbf{x}, s, t) = 0 \text{ and } \det HI(\mathbf{x}, s, t) = I_{xx}(\mathbf{x}, s, t)I_{yy}(\mathbf{x}, s, t) - (I_{xy}(\mathbf{x}, s, t))^2 = 0 \tag{4.9}$$

and as a result top points are the singular points where spatial extrema (where eigenvalues of the Hessian share the same sign) and spatial saddles merge (where eigenvalues of the Hessian have different signs).

On the other hand we need to avoid extreme dislocation of spatial extrema in scale space and instable parts of critical curves. Typically, the slope of the tangent vector along a critical branch $s \mapsto (\mathbf{x}_s^q(t), s)$ in scale space provides a measure on the stability and dislocation. At scale 0 an extremal branch of a strong extremum (i.e. $s_q^*(t) \gg 0$) is nearly vertical whereas at top-point scale $s_q^*(t)$ the slope is horizontal, cf. [11]. Therefore, for each fixed time $t > 0$, we propose the following scale selection per q-th critical branch:

$$\begin{aligned} s_q(t) := \max \Big\{ s = s_{\min} e^{2\tau} \in [0, s_q^*(t)) \;\; | \;\; & \text{for all } s' = s_{\min} e^{2\tau'} \in [0, s) \text{ we have} \\ & \arccos\Big(\frac{\beta}{\sqrt{\| \frac{d}{d\tau}\mathbf{x}_s^q(t)\big|_{\tau=\tau'} \|^2 + \beta^2}}\Big) < \vartheta \Big\} \end{aligned} \tag{4.10}$$

where the tangent vector along the critical curve in scale space is given by

$$\frac{d}{d\tau}\mathbf{x}_s^q(t) = 2s\frac{d}{ds}\mathbf{x}_s^q(t) = -2s[HI(\mathbf{x}_s^q(t), s, t)]^{-1}\Delta\nabla I(\mathbf{x}_s^q(t), s, t),$$

as derived in [36, p.189], where ϑ is an a priori threshold angle, and where β is a parameter with physical dimension [Length] according to the dimensionally consistent, translation and scaling invariant metric tensor

$$\mathrm{d}x \otimes \mathrm{d}x + \mathrm{d}y \otimes \mathrm{d}y + \beta^2 \mathrm{d}\tau \otimes \mathrm{d}\tau = \mathrm{d}x \otimes \mathrm{d}x + \mathrm{d}y \otimes \mathrm{d}y + \beta^2 (2s)^{-2} \mathrm{d}s \otimes \mathrm{d}s$$

that we impose on scale space $\mathbb{R}^2 \times \mathbb{R}^+$ to introduce slope in scale space. In our experiments we set $\beta = (\Delta\tau)^{-1}\sqrt{(\Delta x)^2 + (\Delta y)^2}$, where $\Delta x, \Delta y, \Delta\tau$ denote step-sizes.

In this way the top point scale is discarded in the experiments (by setting $0 < \vartheta \ll \pi/2$), which avoids similar problems as with top points matching and symmetric structures [41] such as the chessboard like structure created by combining frames with horizontal and vertical tags, cf. Figure 2.

Now $s_q(t)$ is the scale of the intersection of the qth extremal branch $s \mapsto (\mathbf{x}_s^q(t), s) \in \mathbb{R}^2 \times \mathbb{R}^+$ and the cilinder $\|\mathbf{x} - \mathbf{x}_0^q(t)\| \leq \delta$, where δ denotes the Euclidean distance between the location of the computed critical point at scale 0, $\mathbf{x}_0^q(t)$, and the projection $(\mathbf{x}_s^q(t), 0)$ at scale 0 of the critical point at scale $s_q(t)$. A simple (but less robust) alternative scale selection would therefore be

$$s_q(t) := \max\{0 < s < s_q^*(t) \mid \forall_{s' \in [0,s)} \|\mathbf{x}_s^q(t) - \mathbf{x}_0^q(t)\| < \tilde{\delta}\} \tag{4.11}$$

where $\tilde{\delta}$ is a threshold on extrema dislocation.

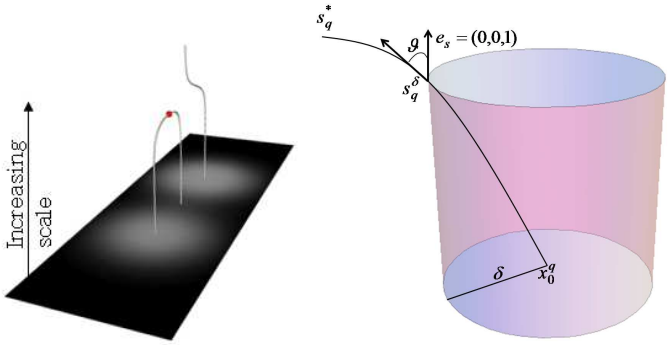

Figure 4: Left image: white lines represent critical paths in scale space (where we keep time t fixed) of certain blobs: $(0, 0, 1)$ direction is the scale direction. The red dot on the critical path is the so-called top-point, Eq. (4.9). Right image: Scale Selection. Scale s_q^* denotes the top point scale. We choose the highest scale s_q such that the slope (in scale space) of the tangent vectors along the part of this critical path below this scale s_q is below a certain a priori angle ϑ. The corresponding spatial dislocation of the critical path (due to diffusion) is denoted by δ.

5 Vector field decomposition

The behavior of cardiac muscle is characterized by twistings and contractions, which can be studied independently by application of the so-called Helmholtz decomposition. In 1858 Helmholtz [23] showed that any vector field, with properties described below, can always be decomposed in *irrotational* and *solenoidal* components. Given a bounded domain $\Omega \subseteq \mathbb{R}^3$ and smooth vector field $\mathbf{v}$, in our case the reconstructed cardiac motion field, $\mathbf{v} \in \mathbf{C}^0(\overline{\Omega})$ and $\mathbf{v} \in \mathbf{C}^1(\Omega)$, where $\overline{\Omega} = \Omega \bigcup \partial\Omega$, there exist functions Φ and $\mathbf{A} \in \mathbf{C}^1(\overline{\Omega})$ such that

$$\mathbf{v}(\mathbf{x}) = \nabla\Phi(\mathbf{x}) + \nabla \times \mathbf{A}(\mathbf{x}) \tag{5.12}$$

and

$$\nabla \cdot \mathbf{A}(\mathbf{x}) = 0 \tag{5.13}$$

where $\mathbf{x} = (x, y) \in \mathbb{R}^3$. In equation (5.21) functions Φ and $\mathbf{A}$ are the so-called *scalar potential* and *vector potential*, whereas $\nabla\Phi(\mathbf{x})$ and $\nabla \times \mathbf{A}(\mathbf{x})$ represent the *irrotational* and *solenoidal* components of vector field

v. However in our cardiac MRI tagging application we consider $\Omega \subseteq \mathbb{R}^2$ and in $\mathbb{R}^2$ one does not have an outer product at hand and therefore we need the following definition and remarks.

Definition 5.1 *Recall that the rotation*[1] *of a vector field in 3D is in Euclidean coordinates expressed as*

$$rot\, \boldsymbol{v} = \nabla \times \boldsymbol{v} = \begin{pmatrix} \partial_y v^3 - \partial_z v^2 \\ \partial_z v^1 - \partial_x v^3 \\ \partial_x v^2 - \partial_y v^1 \end{pmatrix} . \tag{5.14}$$

In this article we define the rotation of a 2D-vector vector field in Euclidean coordinates as follows

$$rot\, \boldsymbol{v} := \partial_x v^2 - \partial_y v^1 . \tag{5.15}$$

and we define the rotation of a scalar field in Euclidean coordinates by

$$\widetilde{rot}\, F := \begin{pmatrix} \partial_y F \\ -\partial_x F \end{pmatrix} \tag{5.16}$$

The theory of Helmholtz decomposition in 3D is easily extended to 2D by replacing the rotation (5.14) consistently by respectively (5.15) and (5.16). For example, the fundamental identity underlying 3D-Helmholtz decomposition is

$$\Delta \mathbf{v} = \operatorname{grad} \operatorname{div} \mathbf{v} - \operatorname{rot} \operatorname{rot} \mathbf{v}$$

which now in 2D becomes

$$\Delta \mathbf{v} = \operatorname{grad} \operatorname{div} \mathbf{v} - \widetilde{\operatorname{rot}} \operatorname{rot} \mathbf{v} .$$

In order to derive an explicit composition (5.21), we derive a solution to the Poisson equation in Ω such that

$$\triangle \boldsymbol{\xi}(\mathbf{x}) = \mathbf{v}(\mathbf{x}) \tag{5.17}$$

by means of

$$\boldsymbol{\xi}(\mathbf{x}) = ((G^{2D} * (1_\Omega v^1))(\mathbf{x}), (G^{2D} * (1_\Omega v^2))(\mathbf{x})) = \int_\Omega G^{2D}(\mathbf{x} - \mathbf{x}')\mathbf{v}(\mathbf{x}')\mathrm{d}\mathbf{x}' \tag{5.18}$$

where 1_Ω denotes the indicator function on Ω and where the fundamental solution for the 2 dimensional Laplacian which is given by

$$G^{2D}(\mathbf{x} - \mathbf{x}') = \frac{1}{2\pi} \ln \|(\mathbf{x} - \mathbf{x}')\| . \tag{5.19}$$

Moreover, $\boldsymbol{\xi}(\mathbf{x})$ satisfies the identity

$$\triangle \boldsymbol{\xi}(\mathbf{x}) = \nabla(\nabla \cdot \boldsymbol{\xi}(\mathbf{x})) - \widetilde{\operatorname{rot}}\, (\operatorname{rot} \boldsymbol{\xi}(\mathbf{x})) \tag{5.20}$$

therefore combining

$$\mathbf{v} = \Delta \boldsymbol{\xi} = \operatorname{grad} \operatorname{div} \boldsymbol{\xi} - \widetilde{\operatorname{rot}} \operatorname{rot} \boldsymbol{\xi} = \operatorname{grad} \Phi + \widetilde{\operatorname{rot}}\, A \tag{5.21}$$

(the 2D equivalent of(5.12)), (5.17) and (5.20), we obtain

$$\Phi(\mathbf{x}) = \nabla \cdot \boldsymbol{\xi}(\mathbf{x}) \text{ and } A(\mathbf{x}) = -\operatorname{rot} \boldsymbol{\xi}(\mathbf{x}). \tag{5.22}$$

However, the decomposition (5.21) is of course not unique. For example if we replace $\boldsymbol{\xi} \mapsto \boldsymbol{\xi} + \mathbf{h}$ with $\mathbf{h}$ some arbitrary Harmonic vector field we have $\Delta(\boldsymbol{\xi} + \mathbf{h}) = \Delta \boldsymbol{\xi} = \mathbf{v}$. Furthermore, if both the divergence

[1] Geometric differential operators such as rotation, divergence and the Laplacian can be introduced coordinate-independently by Hodge-duals and exterior derivatives. This would help avoiding (5.15) and (5.16), but it is beyond the scope of this article.

and rotation of a vector field vanish then this vector field equals the gradient of some Harmonic function. However, the decomposition is unique is we prescribe the field to vanish at the boundary and if moreover we prescribe both the divergence and rotation free part at the boundary, see Lemma 5.1 below. In practice we can not assume that the field vanishes at the boundary, therefor we subtract the Harmonic infilling so that the difference is determined by

$$\begin{aligned}\mathbf{v}(\mathbf{x}) = \nabla \int_\Omega \nabla_{\mathbf{x}} \cdot G^{2D}(\mathbf{x}-\mathbf{x}')\widetilde{\mathbf{v}}(\mathbf{x}')\mathrm{d}\mathbf{x}' - \\ \widetilde{\mathrm{rot}} \int_\Omega \mathrm{rot}_{\mathbf{x}} G^{2D}(\mathbf{x}-\mathbf{x}')\widetilde{\mathbf{v}}(\mathbf{x}')\mathrm{d}\mathbf{x}' + \boldsymbol{\psi}(\mathbf{x})\end{aligned} \tag{5.23}$$

where vector field $\widetilde{\mathbf{v}}(\mathbf{x}) = \mathbf{v}(\mathbf{x}) - \boldsymbol{\psi}(\mathbf{x})$ vanishes at the boundaries, with $\boldsymbol{\psi} = (\mathbf{v}|_{\partial\Omega})_{\mathcal{H}}$ as the unique harmonic infilling (as defined below).

Definition 5.2 *The Harmonic infilling $\boldsymbol{\psi} = (\boldsymbol{v}|_{\partial\Omega})_{\mathcal{H}}$ of the field $\boldsymbol{v}|_{\partial\Omega}$ restricted to the boundary $\partial\Omega$ is by definition the unique solution of*

$$\begin{cases} \triangle\boldsymbol{\psi}(\boldsymbol{x}) = 0 & \boldsymbol{x} \in \Omega \\ \boldsymbol{\psi}|_{\partial\Omega} = \boldsymbol{v}|_{\partial\Omega} \end{cases}$$

As the Helmholtz decomposition (5.21) is not unique, we briefly motivate our particular choice of decomposition (5.23) by the next lemma and subsequent remark.

Lemma 5.1 *Suppose a vector field vanishes at the boundary $\boldsymbol{v}|_{\partial\Omega} = \boldsymbol{0}$ then the divergence free and rotation free part are unique if we prescribe them at the boundary.*

Proof Suppose $\mathbf{v} = \mathbf{v}_1 + \mathbf{v}_2 = \mathbf{u}_1 + \mathbf{u}_2$ with $\mathrm{div}\,\mathbf{v}_1 = \mathrm{div}\,\mathbf{u}_1 = 0$ and $\mathrm{rot}\,\mathbf{v}_2 = \mathrm{rot}\,\mathbf{u}_2 = 0$. Then $\mathrm{div}\,(\mathbf{v}_1 - \mathbf{u}_1) = 0$ and $\mathrm{rot}\,(\mathbf{v}_1 - \mathbf{u}_1) = 0$ so $\mathbf{u}_1 - \mathbf{v}_1 = \nabla h_1$ with $\Delta h_1 = 0$. With similar arguments $\mathbf{u}_2 - \mathbf{v}_2 = \nabla h_2$ with $\Delta h_2 = 0$. Now $\nabla(h_1 + h_2) = \mathbf{0}$ and $\mathbf{v}$ vanishes at the boundary. Consequently, $\Delta(h_1 + h_2) = 0$ and $\frac{\partial(h_1+h_2)}{\partial n}\Big|_{\partial\Omega} = 0$ so $h_1 = -h_2$ and $\mathbf{v}_1 = \mathbf{u}_1 + \nabla h_1$ and $\mathbf{v}_2 = \mathbf{u}_2 - \nabla h_1$ with $\Delta h_1 = 0$. Now as the rotation free and div free part are prescribed we have $(\mathbf{v}_k - \mathbf{u}_k)|_{\partial\Omega} = 0, k = 1, 2$. So $\Delta h_1 = 0$ and $\frac{\partial h_1}{\partial n}\big|_{\partial\Omega} = 0$ and consequently $h_1 = h_2 = 0$ from which the result follows. □

Remark 5.1 *Now a different choice to determine $\boldsymbol{\xi}$ uniquely is to impose $\boldsymbol{\xi}|_{\partial\Omega} = 0$ besides (5.17). This would boil down to*

$$\tilde{\boldsymbol{v}} = \mathit{grad}\,\mathit{div}\,\mathcal{D}\tilde{\boldsymbol{v}} - \widetilde{\mathit{rot}}\;\mathit{rot}\,\mathcal{D}\tilde{\boldsymbol{v}}\;, \tag{5.24}$$

where $\mathcal{D}$ is the Dirichlet operator, i.e $\boldsymbol{\xi} = \mathcal{D}\tilde{\boldsymbol{v}} \Leftrightarrow \Delta\boldsymbol{\xi} = \tilde{\boldsymbol{v}}$ and $\boldsymbol{\xi}|_{\partial\Omega} = \boldsymbol{0}$. However, the Dirichlet kernel on a rectangle, see [28][App.A], is not as tangible (for computation purposes) as the (periodic) convolution operator $\boldsymbol{\xi} = \mathcal{G}\tilde{\boldsymbol{v}} = (G^{2D} * \tilde{v}_1\,1_\Omega, G^{2D} * \tilde{v}_2\,1_\Omega)$ with $\tilde{\boldsymbol{v}} = (\tilde{v}_1, \tilde{v}_2)$ with kernel $G^{2D}(\boldsymbol{x} - \boldsymbol{y})$. Here we note that both $\Delta\mathcal{D} = \Delta\mathcal{G} = I$ and akin to (5.24) we can rewrite (5.23) as

$$\tilde{\boldsymbol{v}} = \mathit{grad}\;\mathit{div}\,\mathcal{G}\tilde{\boldsymbol{v}} - \widetilde{\mathit{rot}}\;\mathit{rot}\,\mathcal{G}\tilde{\boldsymbol{v}}. \tag{5.25}$$

Besides the Dirichlet operator is not a true (periodic) convolution as it is not translation invariant, whereas our choice $\mathcal{G}$ given by (5.18) is translation invariant.

5.1 Multi-scale Helmholtz decomposition of the optical flow field

Instead of using standard derivatives in the Helmholtz decomposition (5.23) and (5.25), we can differentiate the involved Green's functions by Gaussian derivatives, i.e. convolving with a derivative of a Gaussian kernel. In this procedure the kernel is affected by a diffusion, which depending on parameter $s = \frac{1}{2}\sigma^2$, the scale. This diffusion removes the singularity at the origin and, therefore, discretization artefacts. Next we explicitly

compute the diffused first order derivative (with respect to x) of the Green's function by means of Fourier transform of the derivative of the Green's function :

$$\begin{aligned}\partial_x G_s^{2D}(\mathbf{x}) &= \mathcal{F}^{-1}\Big((\omega_1,\omega_2)\mapsto \tfrac{\imath\omega_1}{2\pi(\omega_1^2+\omega_2^2)}\exp(-s(\omega_1^2+\omega_2^2))\Big)(\mathbf{x})\\ &= \mathcal{F}^{-1}\Big((\omega_1,\omega_2)\mapsto \tfrac{\imath\omega_1}{2\pi}\int_s^\infty \exp(-t(\omega_1^2+\omega_2^2))\,\mathrm{d}t\Big)(x,y)\\ &= \int_s^\infty \mathcal{F}^{-1}\Big((\omega_1,\omega_2)\mapsto \tfrac{\imath\omega_1}{2\pi}\exp(-t(\omega_1^2+\omega_2^2))\Big)(x,y)\,\mathrm{d}t\\ &= \int_s^\infty \tfrac{x\exp(-\frac{x^2+y^2}{4t})}{8\pi t^2}\,\mathrm{d}t = \tfrac{x}{2\pi}\tfrac{1-\exp(-\frac{x^2+y^2}{4s})}{x^2+y^2}\end{aligned} \tag{5.26}$$

where ω_1 and ω_2 denote the frequency variables. The derivative of the Gaussian blurred Green's function with respect to y can be calculated using the same approach, hence

$$\partial_y G_s^{2D}(\mathbf{x}) = \frac{y}{2\pi}\frac{1-\exp(-\frac{x^2+y^2}{4s})}{x^2+y^2}\ ,\ \mathbf{x}=(x,y). \tag{5.27}$$

We notice that if the scale $s>0$ tends to zero the diffused/blurred Green function derivatives tend to the ordinary derivatives of the Green's function

$$\begin{aligned}\lim_{s\to 0}\partial_x G_s^{2D}(\mathbf{x}) &= \frac{1}{2\pi}\frac{x}{x^2+y^2}\\ \lim_{s\to 0}\partial_y G_s^{2D}(\mathbf{x}) &= \frac{1}{2\pi}\frac{y}{x^2+y^2}\end{aligned} \tag{5.28}$$

where $\mathbf{x}\neq 0$. Figure 5 shows the graphs of the derivatives of the blurred Green's function $G_s^{2D}(\mathbf{x})$ for $s=0$ and $s=1$. So, in total we get a first improvement over a standard numerical approximation of (5.25) using numerical integration (such as midpoint rule) and finite differences by combining (5.25), (5.26), (5.27) into

$$\tilde{\mathbf{v}}_s := \text{grad}\,(\mathcal{G}_{s,x}\tilde{v}^1+\mathcal{G}_{s,y}\tilde{v}^2) - \widetilde{\text{rot}}\,(-\mathcal{G}_{s,y}\tilde{v}^1+\mathcal{G}_{s,x}\tilde{v}^2). \tag{5.29}$$

with $\mathcal{G}_{s,x^i}\tilde{v}^j := (\partial_{x^i}G_s^{2D} * \tilde{v}_j\,1_\Omega)$, for $i,j=1,2$ with $x^1=x$, $x^2=y$. Now (5.29) still requires to apply differential operators grad and $\widetilde{\text{rot}}$ and we would like to avoid rough finite differences or small scale Gaussian derivatives. Therefore in the next section we combine everything in a single analytic kernel operator, to obtain maximimum accuracy.

5.1.1 Effective analytic convolution operators of the multi-scale Helmholtz decomposition

The Helmholtz decomposition (5.23) and (5.25) can be expressed as a sum of two vector valued convolution kernels that can be pre-computed for computational efficiency. To this end we note that the Helmholtz decomposition commutes with the diffusion operator and we can replace both the div and gradient operator in ∇ by Gaussian derivatives in (5.25). Regarding the first term (rotation free part) we get

$$\nabla^{(\frac{s}{2})}\,\text{div}^{(\frac{s}{2})}\,\mathcal{G}\,\widetilde{\mathbf{v}} = \sum_{i=1}^{2}(\nabla\partial_{x^i}G_{2D}^s * \widetilde{v}^i)(\mathbf{x}) = \sum_{i=1}^{2}(\mathbf{k}_i^{rf,s} * \widetilde{v}^i)(\mathbf{x}) := \sum_{i=1}^{2}((k_i^{rf,s,1} * \widetilde{v}^i)(\mathbf{x}),(k_i^{rf,s,2} * \widetilde{v}^i)(\mathbf{x}))^T\ ,$$

with $x^1=x, x^2=y$, where for example $\nabla^{(\frac{s}{2})}$ denotes the Gaussian gradient at scale $\frac{s}{2}$ given by

$$\nabla^{(\frac{s}{2})}f = \nabla(\phi_{\frac{s}{2}} * f) = (\nabla\phi_{\frac{s}{2}} * f)$$

and where the vector valued convolution kernels $\mathbf{k}_i^{rf,s} = (k_i^{rf,s,1}, k_i^{rf,s,2})^T$, $i=1,2$ are given by

$$\begin{aligned}\mathbf{k}_1^{rf,s}(x,y) = (\nabla\partial_x G_{2D}^s(x,y))^T &= \tfrac{e^{-\frac{x^2+y^2}{4s}}}{4\pi s(x^2+y^2)^2}\begin{pmatrix} -2\left(e^{\frac{x^2+y^2}{4s}}-1\right)s(x^2-y^2)+x^2(x^2+y^2)\\ -4xy\left(e^{\frac{x^2+y^2}{4s}}-1\right)s+xy(x^2+y^2)\end{pmatrix}\ ,\\ \mathbf{k}_2^{rf,s}(x,y) = (\nabla\partial_y G_{2D}^s(x,y))^T &= \tfrac{e^{-\frac{x^2+y^2}{4s}}}{4\pi s(x^2+y^2)^2}\begin{pmatrix} -4xy\left(e^{\frac{x^2+y^2}{4s}}-1\right)s+xy(x^2+y^2)\\ 2\left(e^{\frac{x^2+y^2}{4s}}-1\right)s(x^2-y^2)+y^2(x^2+y^2)\end{pmatrix}\end{aligned} \tag{5.30}$$

for $(x,y) \neq 0$ and $\mathbf{k}_1^{rf,s}(0,0) = (\frac{1}{8\pi}, 0)$ and $\mathbf{k}_2^{rf,s}(0,0) = (0, \frac{1}{8\pi})$. One can apply a similar computation for the divergence free part,

$$(-\widetilde{\text{rot}}^{(\frac{s}{2})} \text{ rot}^{(\frac{s}{2})} \mathcal{G}\tilde{\mathbf{v}})(\mathbf{x}) = \sum_{i=1}^{2} (\mathbf{k}_i^{\text{df},s} * \widetilde{v}^i)(\mathbf{x}) \ ,$$

but it is simpler to use $\phi_s * \tilde{\mathbf{v}} = \nabla^{(\frac{s}{2})} \text{ div}^{(\frac{s}{2})} \mathcal{G}\tilde{\mathbf{v}} - \widetilde{\text{rot}}^{(\frac{s}{2})} \text{ rot}^{(\frac{s}{2})} \mathcal{G}\tilde{\mathbf{v}}$ so that we immediately see that

$$\mathbf{k}_1^{\text{df},s} = (\phi_s - k_1^{\text{rf},s,1}, -k_1^{\text{rf},s,2})^T \text{ and } \mathbf{k}_2^{\text{df},s} = (-k_2^{\text{rf},s,1}, -k_2^{\text{rf},s,2} + \phi_s)^T \tag{5.31}$$

where $\phi_s(\mathbf{x})$ denotes the Gaussian kernel (3.2). So in total we have

$$\sum_{i=1}^{2} (\mathbf{k}_i^{\text{rf},s} * \widetilde{v}^i)(\mathbf{x}) + \sum_{i=1}^{2} (\mathbf{k}_i^{\text{df},s} * \widetilde{v}^i)(\mathbf{x}) = (\phi_s * \tilde{\mathbf{v}})(\mathbf{x}) \ , \tag{5.32}$$

with $s = \frac{1}{2}\sigma^2 > 0$ small (for example $s = 1 \cdot (\text{step size})^2$), where in our algorithms $\mathbf{k}_i^{\text{rf},s}$ and $\mathbf{k}_i^{\text{df},s}$ are analytically precomputed via Eq. (5.30) and Eq. (5.31).

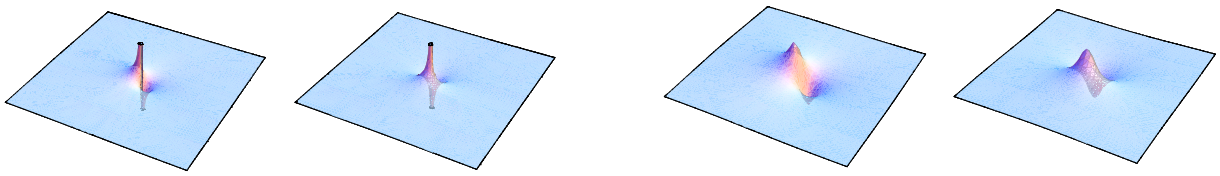

Figure 5: Plots of derivative (5.26) of 2 dimensional Green's function G_s^{2D} with respect to x and y. The two plots on the left display plots of the first order derivatives of the Green's function at scale $s = 0$. The two plots on the right show the case $s > 0$. At scale $s > 0$ the kernel no longer has a singularity at the origin and thereby one avoids sampling errors, grid artefacts and moreover one uses Gaussian-derivatives which are, in contrast to standard derivatives, bounded operators on $\mathbb{L}_2(\mathbb{R}^2)$.

5.2 Experiments on vector field reconstruction

In order to assess the accuracy of the extracted rotation free and divergence free components, as well as the accuracy of the reconstructed vector field, we create a phantom displaying a combination of divergence and rotation, cf. Figure 7 first row. We furthermore compare the performance of the decomposition method described in Section 5.1 and its refinement in Section 5.1.1. The rotation free and divergence free part of the proposed phantom are given by

$$\mathbf{v}(x,y) = \underbrace{(xe_1 + ye_2)\frac{1}{4\pi\gamma}\exp(-\frac{x^2+y^2}{4\gamma})}_{\nabla\Phi_{ideal}} - \underbrace{(ye_1 - xe_2)\frac{1}{4\pi\gamma}\exp(-\frac{x^2+y^2}{4\gamma})}_{\widetilde{\text{rot}}\, A_{ideal}} \tag{5.33}$$

$(x,y) \in [-1,1] \times [-1,1]$, $\gamma = \frac{1}{50}$ (i.e. standard deviation of $\frac{1}{5}$) fixed where $e_1 = (1,0)^T$ and $e_2 = (0,1)^T$ represent a cartesian orthonormal basis. If we apply a diffusion with scale $s > 0$ on the phantom field $\mathbf{v}$ given by (5.33) we obtain the following ground truth analytic multi-scale Helmholtz decomposition

$$\mathbf{v}_s(\mathbf{x}) := (G_s * \mathbf{v})(\mathbf{x}) = -2\gamma \begin{pmatrix} \partial_x \phi_{s+\gamma}(\mathbf{x}) \\ \partial_y \phi_{s+\gamma}(\mathbf{x}) \end{pmatrix} - 2\gamma \begin{pmatrix} -\partial_y \phi_{s+\gamma}(\mathbf{x}) \\ \partial_x \phi_{s+\gamma}(\mathbf{x}) \end{pmatrix}. \tag{5.34}$$

where ϕ_s denotes the Gaussian kernel, recall Eq. (3.2). The decomposition and reconstruction of the phantom's vector field has been carried out at scale $s = 1(\text{step size})^2$ on a equidistant discrete 101×101

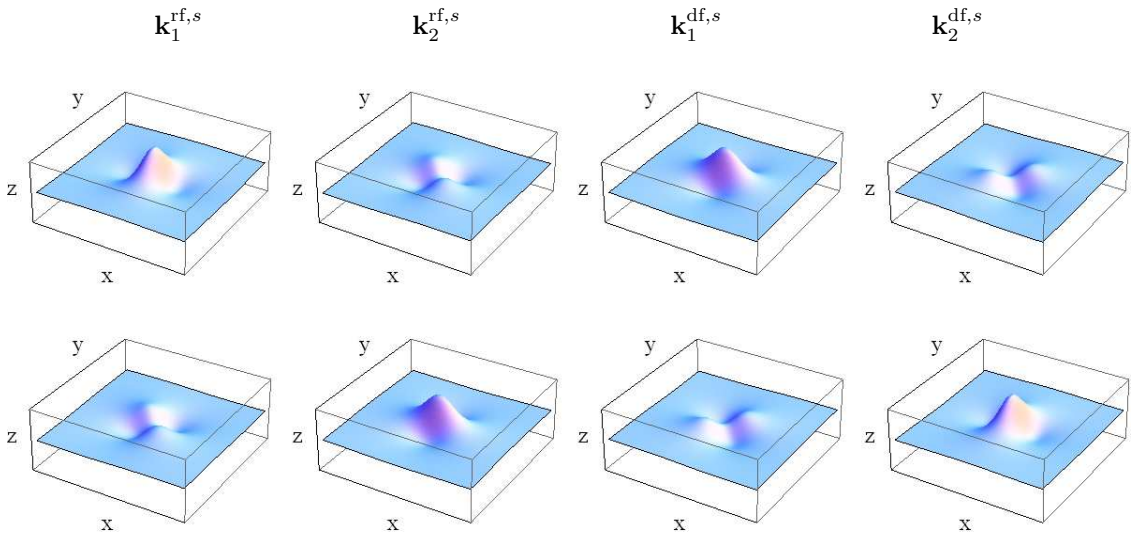

Figure 6: Effective kernels of the multi-scale Helmholtz decomposition (5.32) at a fixed scale $s > 0$. Top row: first component of respectively from left to right $\mathbf{k}_1^{\mathrm{rf},s}, \mathbf{k}_2^{\mathrm{rf},s}, \mathbf{k}_1^{\mathrm{df},s}, \mathbf{k}_2^{\mathrm{df},s}$. Bottom row: second component of respectively from left to right $\mathbf{k}_1^{\mathrm{rf},s}, \mathbf{k}_2^{\mathrm{rf},s}, \mathbf{k}_1^{\mathrm{df},s}, \mathbf{k}_2^{\mathrm{df},s}$.

grid with step size $\frac{1}{50}$ and has been evaluated using error measurements such as the ℓ_∞-norm error and the average angular error (AAE) (5.35) given by

$$AE = \frac{1}{(101)^2} \sum_{i,j=-50}^{50} \arccos\left(\frac{\mathbf{v}_s^{HD}(\mathbf{x}_{ij})}{\|\mathbf{v}_s^{HD}\|} \cdot \frac{\mathbf{v}_s(\mathbf{x}_{ij})}{\|\mathbf{v}_s(\mathbf{x}_{ij})\|}\right), \tag{5.35}$$

$\mathbf{x}_{ij} = \frac{1}{50}(i,j)$, where $\mathbf{v}_s^{HD}$ represents the sum of the divergence free and rotation free part of the Helmholtz-decomposition algorithm and $\mathbf{v}_s$ is the analytically diffused phantom field (ground truth). The proposed algorithm in Section 5.1.1 shows high accuracy in the vector field decomposition; an overview of the error measurements is displayed in table 1, highlighting that the method described in Section 5.1.1 is an improvement of the method described in Section 5.1. In figure 7 we show a comparison between the analytic phantom

	Error Method Section 5.1, Eq. (5.29)		Error Method Section 5.1.1, Eq. (5.32)	
	AAE	ϵ_∞	AAE	rel. ℓ_∞-Norm
Rotation Free Vector Field	$0.35°$	0.28	$1.6° \times 10^{-3}$	1.6×10^{-5}
Divergence Free Vector Field	$0.35°$	0.28	$1.6° \times 10^{-3}$	1.6×10^{-5}
Reconstructed Vector Field	$0.4°$	0.3	$4.3° \times 10^{-4}$	2.0×10^{-5}

Table 1: Performance of the proposed vector decomposition methods (at a fixed scale $s = 1 \cdot (\text{step size})^2$). We used the Average Angular Error (AAE), expressed in degrees and the relative ℓ_∞-norm given by $\epsilon_\infty = \frac{\|\mathbf{v}_s - \mathbf{v}_s^{HD}\|_\infty}{\|\mathbf{v}_s\|_\infty}$, where $\|\mathbf{v}_s\|_\infty = \max_{j\in\{1,2\},\mathbf{x}\in\Omega} |v_s^j(\mathbf{x})|$. Best performances are achieved by method described in Section 5.1.1, Eq. (5.32), showing $AAE = 1.6° \times 10^{-3}$ and $\epsilon_\infty = 1.6 \times 10^{-5}$ for rotation and divergence free components, and $AAE = 4.3° \times 10^{-4}$ and $\epsilon_\infty = 2.0 \times 10^{-5}$ for the reconstructed vector field.

and its components (first row) and the reconstructed vector field and its components (second row).

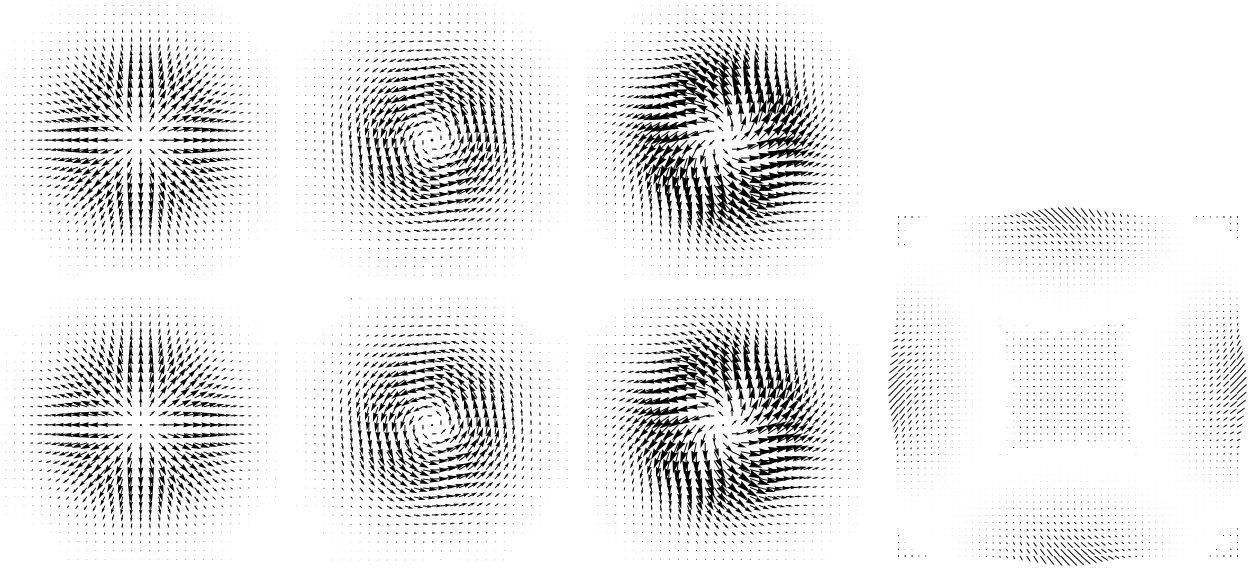

Figure 7: Helmholtz decomposition (top row) of the Phantom field $\mathbf{v}_s$, $s = 1 \cdot (\text{step size})^2$, given by (5.34) and the output $\mathbf{v}_s^{HD}$ of the Helmholtz decomposition algorithm (bottom row, cf. Eq. (5.32)) on domain $[-1,1] \times [-1,1]$. From left to right: the field, rotation free part of the field, diverging free part of the field. Most right image shows the harmonic infilling, Definition 5.2, which we amplified by 10^4 since it is extremely small on $[-1,1] \times [-1,1]$.

6 A brief motivation for using covariant derivatives.

Usually one considers the derivative of a scalar-valued grey-value image (for example the components of a vector-field) $f : \Omega \to \mathbb{R}$ by means of a Gaussian derivative

$$\partial_x^{(s)} f = \partial_x(\phi_s * f) = (\partial_x \phi_s) * f$$

or by a finite difference (i.e. replace first order Gaussian by the discrete $[1,-1]$-stencil filter).

However, there is a short-coming to such an operator. Namely it only compares the *difference* of local luminous intensities $\{f(\mathbf{x}+\mathbf{y}) \mid \|\mathbf{y}\| < 2\sigma\}$ with $f(\mathbf{x})$ and it does not take into account the actual *values* $f(\mathbf{x}+\mathbf{y})$ of local luminous intensities. Basically a directional derivative, say $\partial_x f(\mathbf{x})$ of an image f evaluated at position $\mathbf{x}$ compares the graph of an image locally to the graph of a constant image and we have

$$\partial_x^{(s)}(f) = \partial_x^{(s)}(f + C) \ , \ \text{for all } s > 0 \text{ and all constants } C > 0 \ .$$

In other words the local slope, say in the x-direction, of the graph at $(\mathbf{x}, f(\mathbf{x}))$ is measured by $\partial_x^{(s)}(f)(\mathbf{x})$ is independent of the local hight $f(\mathbf{x})$. Visual perception, however, does not work like this. Consider for example Figure 8. Slope in dark areas are often perceived differently as slopes in light areas. This could be due to the fact that the visual system has some a priori gauge function that it expects due to typical surrounding. If this a priori gauge function is not constant then this gauge-pattern sets an a priori correlation between the slope and hight of the graph of the image.

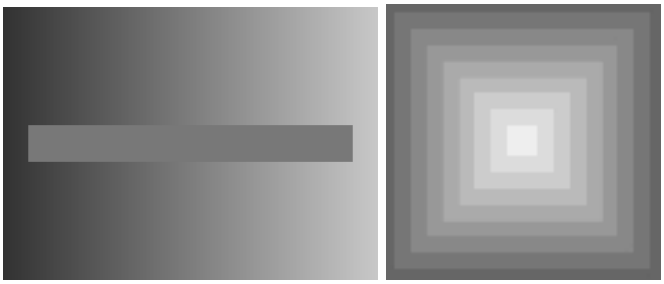

Figure 8: The left-visual illusion illustrates that because of the surrounding grey-values a gradient is perceived in the rectangle, although the rectangle has constant brightness (so computation of a ordinary gradient in the rectangle yields zero). The right visual illusion illustrates the opposite dependence: due to different surrounding gradient structure the same brightness is perceived differently. Along the diagonal cross sections of the square the brightness is perceived higher than along the horizontal cross sections.

We will explain the concept of covariant derivatives of vector fields in Subsection 7. However, in order to provide a road map to covariant derivatives of vector fields in a vector bundle we first explain the covariant derivative of a scalar function $f : \Omega \to \mathbb{R}$ with respect to an a priori gauge function $h : \Omega \to \mathbb{R}$ as introduced by T. Georgiev [17] (in an Adobe Photoshop inpainting application) and subsequently studied in [30, 5]. Such a covariant derivative is given by

$$D^h f(x,y) = Df(x,y) - \frac{1}{h(x,y)}\, Dh(x,y)\, f(x,y) \qquad (x,y) \in \Omega \subset \mathbb{R}^2, \text{ if } h(x,y) \neq 0. \tag{6.36}$$

Note that the covariant derivative is invariant under scalar multiplication of the gauge function, so that

$$D^{\lambda h} f = D^{|h|} f = D^h f \ , \tag{6.37}$$

for all $h \neq 0$. To get a quick preview on the use of covariant derivatives let us return to our visual perception of the gradient in Figure 8 (left figure). As we show in Figure 9 this visual perception can be explained by means of covariant derivatives (and not by standard derivatives).

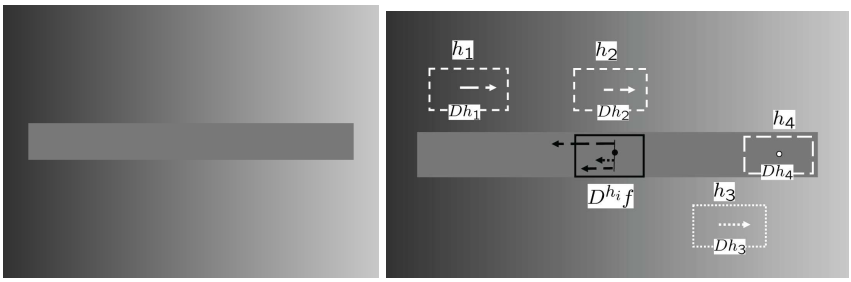

Figure 9: As the rectangle has constant brightness (say 1/2) the visual perception of a gradient can not be explained using standard derivatives, since the regular gradient vanishes within the rectangle. However if we define gauge functions as indicated by white dashed boxes in the image, i.e. $h_i(\tilde{x}, y) = \tilde{x} - x + h_i(\mathbf{0})$ then for points within the rectangle we have $D^{h_i} f(x,y) = Df(x,y) - \frac{1}{h_i(x,y)}\, Dh_i(x,y)\, f(x,y) = \mathbf{0} + \frac{1}{h_i(\mathbf{0})}(-1, 0)$. Here we consistently put the origin of coordinate in the middle of the rectangles. Black vectors indicate covariant gradients whereas white vectors indicate regular gradients. The gauge function/patch index i is indicated by different dashing.

7 Covariant derivatives

Consider the vector[2] bundle

$$E := (\Omega \times \mathbb{R}^2, \pi, \Omega)$$

where $\Omega \subset \mathbb{R}^d$, $d = 2, 3$, is the image domain, where the fundamental projection $\pi : \Omega \times \mathbb{R}^2 \to \Omega$ is given by

$$\pi(x, y, v_1, v_2) = (x, y) \ , \qquad (x, y, v_1, v_2) \in \Omega \times \mathbb{R}. \tag{7.38}$$

The augmented v_1-direction represents the velocity-magnitude in x-direction. The augmented v_2-direction represents the velocity-magnitude in x-direction.

A fiber in this vector bundle is the two dimensional vector space $\pi^{-1}(x, y) = \{(x, y, v_1, v_2) \mid v_1, v_2 \in \mathbb{R}\}$ [3]. A section σ in the vector bundle is the surface which basically represents the graph of some vector-valued function $v : \Omega \to \mathbb{R}^2$:

$$\sigma_{\mathbf{v}}(x, y) = \{(x, y, v_1, v_2) \in \Omega \times \mathbb{R}^2 \mid v_1 = v_1(x, y), v_2 = v_2(x, y)\} \ , \qquad \mathbf{v} = (v^1, v^2)^T,$$

note that $\pi \circ \sigma_{\mathbf{v}} = \mathrm{id}_\Omega$, i.e. $(\pi \circ \sigma_{\mathbf{v}})(x, y) = (x, y)$ for all $(x, y) \in \Omega$, (i.e. σ_v is a section in a vector bundle).

Now that we have set the very basic ingredients for the vector bundle (E, π, Ω). We stress that we do *not* work in the much more common tangent bundle setting $(\Omega \times T(\Omega), \tilde{\pi}, \Omega)$ where sections are vector fields and where $\tilde{\pi}(x, y, \mathbf{v}(x, y)) = (x, y)$. Consequently, we have to rely on the more general concept of covariant derivatives in vector bundle rather than the covariant derivative in the tangent bundle, which we explain next.

7.1 A Tool from Differential Geometry: Connections on the Vector Bundle E

A connection on a vector bundle is by definition a mapping $D : \Gamma(E) \to \mathcal{L}(\Gamma(T(\Omega)), \Gamma(E))$ from the space of sections in the vector bundle $\Gamma(E)$ to the space of linear mappings $\mathcal{L}(\Gamma(T(\Omega)), \Gamma(E))$ from the space of vector fields on Ω denoted by $\Gamma(T(\Omega))$ into the space of sections $\Gamma(E)$ in the vector bundle E such that

$$\begin{aligned} &D_{\mathbf{v}+\mathbf{w}}\sigma = D_{\mathbf{v}}\sigma + D_{\mathbf{w}}\sigma \ , \\ &D_{f\mathbf{v}}\sigma = f D_{\mathbf{v}}\sigma \ , \\ &D_{\mathbf{v}}(\sigma + \tau) = D_{\mathbf{v}}\sigma + D_{\mathbf{v}}\sigma \ , \\ &D_{\mathbf{v}}(f\sigma) = \mathbf{v}(f)\sigma + f D_{\mathbf{v}}\sigma \end{aligned} \tag{7.39}$$

for all vector fields $\mathbf{v} = \sum_{i=1}^2 v^i \partial_{x^i}, \mathbf{w} = \sum_{i=1}^2 w^i \partial_{x^i} \in \Gamma(T(\Omega))$ (i.e. sections in tangent bundle $T(\Omega)$) and all $f \in C^\infty(\Omega, \mathbb{R})$ and all sections $\sigma \in \Gamma(E)$ in the vector bundle E. Note that we used the common short notation $D_{\mathbf{v}}\sigma = (D\sigma)(\mathbf{v})$. One can verify that (7.39) implies that

$$\begin{aligned} ((D\sigma_{\mathbf{v}})(X))(\mathbf{c}(t)) \ &= D(v^1\sigma_1 + v^2\sigma_2)(X)(\mathbf{c}(t)) \\ &= \sum_{j=1}^2 X|_{\mathbf{c}(t)}(v^j)\ \sigma_j + \sum_{j=1}^2 \sum_{i=1}^2 v^j(\mathbf{c}(t))\, \dot{c}^i(t)\ (D_{\partial_{x^i}}\sigma_j)(\mathbf{c}(t)) \ \in \Gamma(E), \end{aligned} \tag{7.40}$$

where $\sigma_1(x, y) = (x, y, 1, 0)$ and $\sigma_2(x, y) = (x, y, 0, 1)$ denote the unit sections in x and y-direction and where $X|_{\mathbf{c}(t)} = \sum_{i=1}^2 \dot{\mathbf{c}}^i(t)\ \partial_{x^i}|_{\mathbf{c}(t)}$ denotes a vector field on Ω tangent to a curve $\mathbf{c} : (0, 1) \to \Omega$ is a smooth curve in the image domain $\Omega \subset \mathbb{R}^2$, with $\dot{\mathbf{c}}(t) = \frac{d}{dt}\mathbf{c}(t)$ and components $\mathbf{c}^i(t) = \langle \mathrm{d}x^i, \dot{\mathbf{c}}(t)\rangle$ obtained by the dual basis vector fields $\mathrm{d}x^1, \mathrm{d}x^2$ in the co-tangent bundle $T^*(\Omega)$.

Formula (7.40) tells us that the connection is entirely determined by its output on the (constant) basis sections σ_j and the basis vector fields ∂_{x^i}, i.e. D is uniquely determined by $\{D_{\partial_{x^i}}\sigma_j\}_{i,j=1,2}$. Now for each $i, j = 1, 2$ this output $D_{\partial_{x^i}}\sigma_j$ is a section and consequently there exist unique functions $\Gamma_{ij}^k : \Omega \to \mathbb{R}$ (Christoffel-symbols) such that

$$(D_{\partial_x^i}\sigma_j)(\mathbf{c}(t)) = \Gamma_{ij}^k(\mathbf{c}(t))\sigma_k \ .$$

[2] In previous work we called $(\mathbb{R}^2 \times \mathbb{R}^+, \pi, \Omega)$ a vector bundle, but formally speaking this is not right $\mathbb{R}^+$ is not a vector space.

[3] Here we stress that we do *not* assume that this two dimensional vector space is the tangent space $T_{(x,y)}(\Omega)$, since our vector bundle is not a tangent bundle

7.2 Covariant derivatives on the Vector Bundle E induced by gauge fields.

In this article we restrict ourselves to the diagonal case (no interaction between the components)

$$\Gamma_{ij}^k = A_i^k \, \delta_j^k \ , \text{ with } A_i^k := \Gamma_{ik}^k, \tag{7.41}$$

We impose this restriction for pragmatic reasons: It keeps the implementation relatively simple. Moreover, this choice is a straightforward generalization of our previous work on reconstruction of scalar valued functions using covariant derivatives [30]. Although this choice does not affect the rules for covariant derivatives on a vector bundle (7.39), this restriction may not be a necessary.

Consequently, we have

$$\begin{array}{l} (Dv^1\sigma_1)(\partial_{x^i}) = (\partial_{x^i}v^1 + A_i^1\, v^1)\,\sigma_1 \ , \text{ for } i = 1,2. \\ D_{\partial x^i}\sigma_{\mathbf{v}} = (D\sigma_{\mathbf{v}})(\partial_{x^i}) = (\partial_{x^i}v^1 + A_i^1\, v^1)\,\sigma_1 + (\partial_{x^i}v^2 + A_i^2\, v^2)\,\sigma_2 \text{ with } \mathbf{v} = \sum_{i=1}^2 v^i\sigma_i \in \Gamma(E) \end{array} \tag{7.42}$$

Now the next step is to choose $\{A_i^j\}$ such that an a priori given section $\sigma_{\mathbf{h}}$ (a so-called *gauge-field*, [30])

$$(x,y) \mapsto \sigma_{\mathbf{h}}(x,y) \text{ with } \sigma_{\mathbf{h}}(x,y) = (x,y,h^1(x,y),h^2(x,y)) \ , \mathbf{h} = (h^1,h^2)^T,$$

is "invisible" with respect to the covariant derivative, i.e. we must solve for

$$\begin{array}{l} (D\sigma_{\mathbf{h}})(\partial_{x^i}) = 0 \text{ for all } i = 1,2 \ \Leftrightarrow \\ (\partial_{x^i}h^1 + A_i^1h^1)\,\sigma_1 + (\partial_{x^i}h^2 + A_i^2h^2)\,\sigma_2 = 0\,\sigma_1 + 0\,\sigma_2 \text{ for all } i = 1,2 \ \Leftrightarrow \\ A_i^j = -\frac{\partial_{x^i}h^j}{h^j} \text{ for all } i,j = 1,2, \end{array} \tag{7.43}$$

so that the covariant derivative $D^{\mathbf{h}}$ induced by gauge-field $\sigma_{\mathbf{h}} \in \Gamma(E)$ is given by

$$\begin{array}{rl} (D^{\mathbf{h}}_{\partial x^i}\sigma_{\mathbf{v}})(\mathbf{x}) & = (\partial_{x^i}v^1(\mathbf{x}) - \frac{\partial_{x^i}h^1(\mathbf{x})}{h^1(\mathbf{x})}\, v^1(\mathbf{x}))\,\sigma_1 + (\partial_{x^i}v^2(\mathbf{x}) - \frac{\partial_{x^i}h^2(\mathbf{x})}{h^2(\mathbf{x})}\, v^2(\mathbf{x}))\,\sigma_2 \\ & = ((\partial_{x^i})^{h_1})(\mathbf{x})\,\sigma_1 + ((\partial_{x^i})^{h_2})(\mathbf{x})\,\sigma_2 \ . \end{array}$$

Now that we introduced everything in a formal differential geometry setting we will simplify our notations. In the remainder of this article, we will identify sections $\sigma_{\mathbf{v}}$ in E with the corresponding vector-functions $\mathbf{v} : \Omega \to \mathbb{R}^2$

$$\begin{array}{lcl} \sigma_{\mathbf{v}=v^1,v^2}(\mathbf{x}) = (\mathbf{x}, v^1(\mathbf{x}), v^2(\mathbf{x})) & \leftrightarrow & \mathbf{v}(\mathbf{x}) = (v^1(\mathbf{x}), v^2(\mathbf{x}))^T \ , \text{ for all } \mathbf{x} \in \mathbb{R}^2, \\ \sigma_1 = (0,0,1,0) & \leftrightarrow & \mathbf{e}_1 := (1,0)^T \ , \\ \sigma_2 = (0,0,0,1) & \leftrightarrow & \mathbf{e}_2 := (0,1)^T \ . \end{array} \tag{7.44}$$

and briefly write $\partial^{\mathbf{h}}_{x^i}\mathbf{v} : \Omega \to \mathbb{R}^2$ for the vector function corresponding to the section $D^{\mathbf{h}}_{\partial x^i}\sigma_{\mathbf{v}} : \Omega \to E$, i.e. :

$$(x, y, \partial^{\mathbf{h}}_{x^i}\mathbf{v}(x,y)) = (D^{\mathbf{h}}_{\partial x^i}\sigma_{\mathbf{v}})(x,y) \ .$$

where we applied short notation $\partial^{\mathbf{h}}_{x^i}\mathbf{v} := D^{\mathbf{h}}_{\partial x^i}\sigma_{\mathbf{v}}$.

Note that covariant derivatives are invariant under sign-transitions.

$$A_i^j = -\frac{\partial_{x^i}h^j}{h^j} = -\frac{\partial_{x^i}|h^j|}{|h^j|} \text{ for all } i,j = 1,2. \tag{7.45}$$

The covariant Laplacian can be explicitly expressed in components

$$\begin{array}{rl} (D^{\mathbf{h}})^*D^{\mathbf{h}}\mathbf{v} & = \sum_{j=1}^2\sum_{i=1}^2 \left(\left(\partial^{h^j}_{x^i}\right)^* \partial^{h^j}_{x^i} v^j\right)\mathbf{e}_j, \\ & = \sum_{j=1}^2 \left(-\Delta v^j + \frac{\Delta h^j}{h^j}v^j\right)\mathbf{e}_j \end{array} \tag{7.46}$$

where we recall our identifications (7.44). With respect to this covariant Laplacian we recall that

$$(\partial_{x^i})^{h^j} v^j = \partial_{x^i} v^j - \frac{\frac{\partial h^j}{\partial x^i}}{h^j} v^j \tag{7.47}$$

so that its $\mathbb{L}_2$-adjoint defined by

$$\Big((\partial_{x^i})^{h^j} v^j, \phi\Big)_{\mathbb{L}_2(\Omega)} = \Big(\phi, \Big((\partial_{x^i})^{h^j}\Big)^* v^j\Big)_{\mathbb{L}_2(\Omega)} \text{ for all } \phi \in \mathbb{L}_2(\Omega),$$

is given by

$$\Big((\partial_{x^i})^{h^j}\Big)^* v^j = -\partial_{x^i} v^j - \frac{\partial_{x^i} h^j}{h^j} v^j \ . \tag{7.48}$$

If we compare the adjoint covariant derivative to the covariant derivative we see that the multiplicator part is maintained whereas the derivative-part contains an extra minus sign. So that indeed by straightforward computation one finds the fundamental formula:

$$\begin{aligned} \sum_{i=1}^2 \Big(\partial_{x^i}^{h^j}\Big)^* \partial_{x^i}^{h^j} v^j &= \sum_{i=1}^2 -\tfrac{\partial}{\partial x^i} \big(\tfrac{\partial}{\partial x^i}\big)^{h^j} v^j - \frac{\frac{\partial h^j}{\partial x^i}\big(\frac{\partial}{\partial x^i}\big)^{h^j} v^j}{h^j} \\ &= \sum_{i=1}^2 -\tfrac{\partial}{\partial x^i}\Big(\tfrac{\partial v^j}{\partial x^i} - \tfrac{\partial h^j}{\partial x^i}\tfrac{v^j}{h^j}\Big) - \frac{\frac{\partial v^j}{\partial x^i}\Big(\frac{\partial v^j}{\partial x^i} - \frac{\partial h^j}{\partial x^i}\frac{v^j}{h^j}\Big)}{h^j} \\ &= -\Delta v^j + \tfrac{\Delta h^j}{h^j} v^j. \end{aligned} \tag{7.49}$$

Now, that we have introduced the covariant Laplacian we mention two preliminary issues that directly arise from (7.49) and which will be addressed in the remainder of this article.

Remark 7.2 *At first sight the covariant derivatives and their associated (inverse) Laplacian, seem to be numerically ill-posed as the gauge-field components should not vanish, likewise in the previous works [17, 30, 5]. However, the crucial scaling property of covariant derivatives, Eq. (6.37) allows us to scale away from* 0 *and numerical singular behavior is avoided by adding a tiny* $0 < \delta \ll 1$ *in the computation of*

$$\frac{\Delta h^j(x,y)}{h^j(x,y)} \approx \frac{\Delta h^j(x,y) + \delta}{h^j(x,y) + \delta} = -\Delta(-\log|h^j(x,y) + \delta|) + \|\nabla \log|h^j(x,y) + \delta|\|^2.$$

Furthermore, as we will see later in Section 7.3, regarding stability, the Dirichlet kernel of the coercive *covariant Laplacian behaves similar to the Dirchlet kernel of the regular Laplacian (with the advantage that it locally adapts to concave and convex behavior of the gauge function). Finally, we will show how the manifest stability of our algorithms, depends on the choice of gauge field.*

Remark 7.3 *Covariant derivatives of sections (vectorvalued functions) in the vector bundle E given by (7.42) in general do not coincide with covariant derivatives of sections (vector fields) in $((\Omega, T(\Omega)), \tilde{\pi}, \Omega)$. The components in (7.47) are coordinate dependent and not compatible with respect to orthogonal coordinate transformations (such as rotations). This incompatibility is due to our restriction (7.41) and we return to this issue in Section 8.*

7.2.1 Interpolation between conventional derivatives and covariant derivatives

In this section we briefly explain that a monotonic transformation on the components of the gauge field takes care of the interpolation between standard derivatives and covariant derivatives. For the sake of illustration we restrict ourselves to the scalar valued case (with positive gauge function $h : \Omega \to \mathbb{R}^+$, recall (7.45)) as the vector valued case follows by applying everything on the two separate components. By applying a the monotonic transformation $h \mapsto h^\eta$ on the gauge function we obtain the following covariant derivative

$$D^{h^\eta} f = f - D(\log h^\eta) f = f - \eta (D \log h) f \ . \tag{7.50}$$

If $\eta = 0$ the expression (7.50) provides a conventional derivative, whereas the case $\eta = 1$ yields a covariant derivative with respect to gauge function h.

On the one hand we want to preserve the influence of the gauge field (initial guess) h. On the other hand outliers in the magnitude of the gauge field h get too much influence in the final reconstruction if $\eta \geq 1$. Furthermore we have to keep track of error-propagation[4] where η should neither be too large nor too small. So we observe a trade-off situation for the choice of η in our application. This will also appear in the experimental section, Section 10, Figure 15.

7.3 Fundamental properties of the self-adjoint covariant laplacian

In this section we shall show that covariant Laplacian has more or less the same fundamental properties as the ordinary Laplacian. These basic fundamental properties include self-adjointness, negative definiteness and coercivity, that are important for wellposed symmetric inverse problems that shall arise from Euler Lagrange equations for vector field interpolation later on in Section 8 and Section 9.

Definition 7.3 *Let H be a Hilbert space with inner product $(\cdot,\cdot)$. An unbounded operator $A : H \to H$ on a Hilbert space H with domain $\mathcal{D}(A)$ is self-adjoint if*

$$(Af, g) = (f, Ag) \text{ for all } f, g \in \mathcal{D}(A) \ ,$$

and if the domain of the adjoint $\mathcal{D}(A^*)$ coincides with the domain of A, i.e. $\mathcal{D}(A^*) = \mathcal{D}(A)$. Such an operator is coercive if there exists a positive constant $c > 0$ s.t.

$$(Af, f) \geq c(f, f)$$

for all $f \in \mathcal{D}(A)$.

Now suppose that the gauge field is twice continuously differentiable and suppose that the multipliers

$$\frac{\Delta h^j}{h^j}, j = 1, 2 \text{ are bounded.} \tag{7.51}$$

Then the covariant Laplacian is just like the ordinary Laplacian an unbounded negative definite operator on $\mathbb{L}_2(\Omega)$ with domain

$$\mathcal{D}\left(\sum_{i=1,2}\left(\partial_{x^i}^{h^j}\right)^* \partial_{x^i}^{h^j}\right) = \mathbb{H}_2^0(\Omega) := \{f \in \mathbb{H}_2(\Omega) \ : \ f|_{\partial\Omega} = 0\}. \tag{7.52}$$

Note that $\partial_{x^i}^{h^j}$ is not even a normal operator

$$\left(\partial_{x^i}^{h^j}\right)^* \partial_{x^i}^{h^j} \neq \partial_{x^i}^{h^j}\left(\partial_{x^i}^{h^j}\right)^*.$$

The covariant Laplacian operator $\left(\partial_{x^i}^{h^j}\right)^* \partial_{x^i}^{h^j}$ is negative definite

$$-\left(\sum_{i=1,2}\left(\partial_{x^i}^{h^j}\right)^* \partial_{x^i}^{h^j} f, f\right)_{\mathbb{L}_2(\Omega)} = \left(\partial_{x^i}^{h^j} f, \partial_{x^i}^{h^j} f\right)_{\mathbb{L}_2(\Omega)} > 0$$

for all f with[5] $f \neq 0$ regardless the choice of h^j as long as $\frac{\Delta h^j}{h^j}$ is bounded, which we will assume form now on. Now by assumption the gauge field is twice differentiable and as a result $\frac{\Delta h^j}{h^j}$ is continuous on a compact domain Ω, so there exists some $\mathbf{x}_0^j \in \Omega$ such that

$$-\frac{\Delta h^j}{h^j} \leq -\frac{\Delta h^j(\mathbf{x}_0^j)}{h^j(\mathbf{x}_0^j)}. \tag{7.53}$$

[4]The condition number associated with linear system (8.75) describes the error propagation.

[5]Note that $f \in \mathbb{H}_2^0$ with $\partial_{x^i}^{h^j} f = 0$ implies that f is scalar multiple of h^j which violates our assumption (7.51) if $f \neq 0$.

Now minus the covariant Laplacian is an operator of Sturm-Liouville (p,q)-type [24] with $p=1$ and $q=q_j:=-\frac{\Delta h^j}{h^j}$, recall Eq. (7.49), with $q^j\leq q(\mathbf{x}_0^j)$. Consequently, the covariant Laplacian is self-adjoint and the corresponding self-adjoint resolvent operator

$$\left(I-\sum_{i=1,2}\left(\partial_{x^i}^{h^j}\right)^*\left(\partial_{x^i}^{h^j}\right)\right)^{-1} \tag{7.54}$$

is compact and thereby there exists a complete orthonormal set of strictly positive eigenvalues and eigenfunctions [42, Thm 13.33] such that

$$\left\{\begin{array}{rl} -\sum_{i=1,2}\left(\partial_{x^i}^{h^j}\right)^*\left(\partial_{x^i}^{h^j}\right)f_n^j &= \lambda_n^j f_n^j\ , j=1,2,\\ f_n^j\big|_{\partial\Omega} &= 0, j=1,2,\end{array}\right. \Leftrightarrow \left\{\begin{array}{rl} \Delta(f_n^j)+q_j\ f_n^j &= \lambda_n^j f_n^j\ j=1,2,\\ f_n^j\big|_{\partial\Omega} &= 0,\ j=1,2,\end{array}\right.$$

where we stress that $\lambda_n=0$ would yield the trivial solution only, as $D^{h^j}f^j=0$ implies $f^j=\lambda h^j$ which for $\lambda\neq 0$ would contradict (7.53) since $f_n^j\big|_{\partial\Omega}=0$. Now the resolvent of the covariant Laplacian is compact with a domain $\mathbb{H}_2^0(\Omega)$ that is compactly embedded in $\mathbb{L}_2(\Omega)$ and consequently, 0 is the *only* density point of the spectrum of the resolvent. Consequently, the spectrum of the minus covariant Laplacian is contained in

$$\sigma\left(-\sum_{i=1,2}\left(\partial_{x^i}^{h^j}\right)^*\partial_{x^i}^{h^j}\right)\subset[c_h(\Omega),\infty)$$

for some $c_h(\Omega)>0$ and by the Sturm-Liouville theory [19] the spectrum only consists of eigenvalues so that $c_h(\Omega)$ equals the smallest eigen value $\lambda_1^j(\mathbf{h})$ of the covariant Laplacian restricted to its domain (7.52) which can be expressed by the Rayleigh quotient

$$\lambda_1^j(\mathbf{h}) \ = \min_{\mathbf{f}\in\mathbf{H}_2^0(\Omega)}\frac{\sum_{j=1,2}\int_\Omega -f^j(\mathbf{x})\Delta f^j(\mathbf{x})+q^j(\mathbf{x})f^2(\mathbf{x})\ \mathrm{d}\mathbf{x}}{\sum_{j=1,2}\int_\Omega (f^j)^2(\mathbf{x})\mathrm{d}x}=\min_{\mathbf{f}\in\mathbf{H}_2^0(\Omega)}\frac{\sum_{j=1,2}\int_\Omega (\nabla f^j\cdot\nabla f^j)(\mathbf{x})+q^j(\mathbf{x})f^2(\mathbf{x})\ \mathrm{d}\mathbf{x}}{\sum_{j=1,2}\int_\Omega\ (f^j)^2(\mathbf{x})\mathrm{d}x}\ .$$

We conclude that the covariant Laplacian is just like the regular Laplacian a coercive operator on the domain $\mathbb{H}_2^0(\Omega)$ with a complete orthogonal basis of eigenfunctions. This coercivity is important for the stability of the numerical algorithms (via the Lax-Milgram theorem, [37]) later on, since inverting the covariant Laplacian boils down to inverting all the eigenvalues.

Remark 7.4 *The smallest eigen value $\lambda_1(\boldsymbol{1})$ in case of a constant gauge field corresponds to the Poincaré constant [50] of the regular Laplacian with domain $\mathbb{H}_0^2(\Omega)$. In case of a rectangular domain, $\Omega=[0,M]\times[0,L]$ we have*

$$\lambda_1^j(\boldsymbol{1})=\pi^2\left(\frac{1}{M^2}+\frac{1}{L^2}\right)\ ,$$

since the eigen functions of the regular Laplacian on the rectangle $\Omega=[0,M]\times[0,L]$ with domain $\mathbb{H}_2^0(\Omega)$ are given by

$$\{\sin\left(\frac{mx\pi}{M}\right)\sin\left(\frac{ny\pi}{L}\right)\ |\ m,n=1,2,\ldots\}$$

with corresponding eigen values $\pi^2\left(\frac{m^2}{M^2}+\frac{l^2}{L^2}\right)$. However, since the q^j need not be positive, it in general is hard to derive an explicit formula for the lower bound for the smallest eigenvalues of the covariant Laplacian with domain $\mathbb{H}_2^0(\Omega)$.

In general it is apparent from the essential formula (7.49), that the more convex the gauge field, the more well-posed the inversion of the covariant Laplacian and the covariant resolvent (7.54) is. See the typical Example 1 and Example 2 below, where we respectively consider basic gauge fields that are convex and

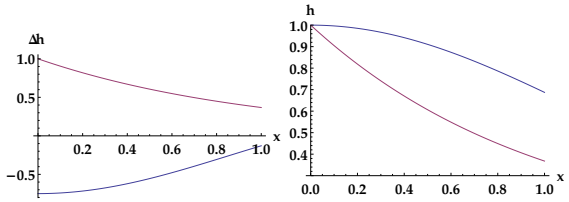

Figure 10: The graphs of the gauge functions and corresponding Laplacian in Example 1 (convex case, $\gamma = 1$, in red) and Example 2 (concave case, $\alpha = \frac{3}{8}$, in blue).

mainly locally concave. As the covariant Laplacian (7.49) of a vector field acts componentwise, we will (for the sake of simple illustration) consider examples of a covariant Laplacian

$$(D^h)^* D^h f = -\Delta f + \frac{\Delta h}{h} f$$

of a *scalar field* f with respect to a *scalar field* h. See Figure 10. Here the reader should keep in mind that in the applications later on f is the component of a vector field $\mathbf{v}$ and h is a component of the gauge field $\mathbf{h}$.

Example 1 *Consider the case where* $\Omega = [0,1] \times [0,1]$ *and* $h(x,y) = \lambda\, e^{-\gamma(x+y)}$*, with* $\gamma \geq 0$*,* $\lambda \neq 0$*, then*

$$\frac{\Delta h}{h} = \gamma^2 \geq 0$$

and we have $(D^h)^* D^h = -\Delta + \gamma^2\, I$ *and the smallest eigenvalue of the covariant Laplacian equals is* $2\pi^2 + \gamma^2$*, which shows that the covariant Dirichlet problem is better posed than a regular Dirichlet problem in case of a convex gauge field.*

In our applications the gauge-field usually is a superposition of Gaussians. Typically Gaussians inhibit concave areas around the mean. To investigate the influence of these concave areas on the stability of inverse problems based on covariant Laplacians we consider the following example.

Example 2 *Consider the case where* $\Omega = [0,1] \times [0,1]$ *and the gauge function is a Gaussian kernel* $h(x,y) = \lambda(\frac{1}{2\pi\sigma^2} e^{-\frac{(x^2+y^2)}{2\sigma^2}})$*, with* $\lambda > 0$ *arbitrary, then the Gaussian kernel is concave for* $x^2 + y^2 < 2\sigma^2$*. For convenient computation set* $\alpha := \frac{1}{2\sigma^2} = \frac{3}{8}$ *in which case the gauge function is concave on* Ω*, see Figure 10. A brief computation yields* $q(x,y) = \frac{\Delta h(x,y)}{h(x,y)} = 4\alpha(\alpha(x^2+y^2) - 1)$ *and if we now apply the standard method of separation on* $-\Delta + q$ *we find*

$$\mu_1 + \mu_2 - 4\alpha = \frac{4\alpha^2 x^2 X(x) - X''(x)}{X(x)} - \frac{4\alpha^2 y^2 Y(y) - Y''(y)}{Y(y)} - 4\alpha = \lambda$$

with $X(0) = X(1) = 0$ *and* $Y(0) = Y(1) = 0$*. So set* $X(x) = e^{-\alpha x^2} \tilde{X}(2\sqrt{\alpha}x)$ *and* $Y(y) = e^{-\alpha y^2} \tilde{Y}(2\sqrt{\alpha}y)$ *and set* $\xi = 2\sqrt{\alpha}x$ *and* $\eta = 2\sqrt{\alpha}y$ *then we arrive at the Hermite differential equation*

$$\begin{aligned} &\tilde{X}''(\xi) - 2\xi\tilde{X}'(\xi) - \tfrac{1}{2}\tilde{X}(\xi) = -\tfrac{\mu_1}{2\alpha}\tilde{X}(\xi)\ , \\ &\tilde{X}(0) = \tilde{X}(2\sqrt{\alpha}) = \tilde{X}\left(\sqrt{\tfrac{3}{2}}\right) = 0 \end{aligned}$$

and an analogous Hermite differential equation for $\tilde{Y}(\eta)$*. Now we arrive at the Hermite polynomials* $H_n(x)$ *of order* n*, where the lowest order that could possibly fit the boundary conditions is* $n = 3$*. So*

$$\frac{\mu_1}{2\alpha} - \frac{1}{2} = 6 = 2n \Rightarrow \mu_1 = 13\alpha\ ,$$

and the eigen function with smallest eigenvalue of the covariant Laplacian is

$$e^{-\alpha(x^2+y)^2} H_3(-2\sqrt{\alpha}x) H_3(-2\sqrt{\alpha}y)$$

with eigenvalue $\lambda = \mu_1 + \mu_2 - 4\alpha = 26\alpha - 4\alpha = 22\alpha \approx 8.25$ *which is less than* $\pi^2 \approx 9.87$*, but the difference is rather small.*

7.3.1 The Green's function of the covariant Laplacian and an explicit coercivity bound

Although that the coercivity constant $c_h(\Omega)$ is harmless in Example 1 and Example 2, it does not say much on the general case where the coercivity constant depends on the gauge function $h : [0,1] \times [0,1] \to \mathbb{R}^+$. In the general case, where $h \in C^2([0,1] \times [0,1])$ is arbitrary, we can get a grip on the coercivity constant $c_h(\Omega)$ by considering the Green's function of the covariant Laplacian. Here we employ the decomposition $-\Delta f + \frac{\Delta h}{h} f = (D^h)^* D^h f$ and we partially follow Sturm-Liouville theory, which does not fully apply since $h^{-1}\Delta h$ need not be positive. To obtain the coercivity constant for $(D^h)^* D^h$ we may restrict ourselves to the 1 dimensional case since

$$(-\Delta + \frac{\Delta h}{h})f = -\frac{\partial^2 f}{\partial x^2} + \frac{\frac{\partial^2 h}{\partial x^2}}{h} f - \frac{\partial^2 f}{\partial y^2} + \frac{\frac{\partial^2 h}{\partial y^2}}{h} f = \sum_{i=1}^{2} \left(\frac{\partial^h}{\partial x^i}\right)^* \left(\frac{\partial^h}{\partial x^i}\right) f,$$

so that if we find a lower-bound $\tilde{c}_{\tilde{h}}([0,1])$ on the 1D- covariant Laplacian

$$\mathbb{H}_0^2([0,1]) \ni \tilde{f} \mapsto D^{\tilde{h}} \tilde{f} = -\tilde{f}'' + \frac{\tilde{h}''}{\tilde{h}} \tilde{f} \in \mathbb{L}_2(0,1) \ ,$$

then by means of the estimate

$$\int_0^1 \int_0^1 \left| \frac{\partial^h f(x,y)}{\partial x} \right|^2 \mathrm{d}x\mathrm{d}y \geq \int_0^1 \tilde{c}_{h(\cdot,y)}([0,1]) \int_0^1 |f(x,y)|^2 \, \mathrm{d}x \, \mathrm{d}y$$

we obtain the following lower bound on the 2D covariant Laplacian

$$-\Delta + \frac{\Delta h}{h} > c_h([0,1] \times [0,1]) := \min_{x \in [0,1]} \{\tilde{c}_{h(x,\cdot)}([0,1])\} + \min_{y \in [0,1]} \{\tilde{c}_{h(\cdot,y)}([0,1])\}. \tag{7.55}$$

Therefore, in the remainder of this subsection and Appendix A we consider the 1D gauge function h and 1D input function f and for the sake of sober notation we thereby omit the tildes and write $h \in C^2(0,1)$ with $h > 0$ and $f \in \mathbb{L}_2(0,1)$. However, we actually consider the cases $\tilde{h}(x) = h(x,y)$ and $\tilde{f}(x) = f(x,y)$ for a fixed y or $\tilde{h}(y) = h(x,y)$ and $\tilde{f}(y) = f(x,y)$ for a fixed x in (7.55).

In Appendix A we show that the Green's function of the 1D covariant Laplacian $f \mapsto (D^h)^* D^h f = -f'' + \frac{h''}{h} f$ is given by

$$k_h(x,y) = \frac{h(x)h(y)}{Q_h(1)} \cdot \begin{cases} Q_h(x)(Q_h(1) - Q_h(y)) & \text{for } x \leq y \ , \\ Q_h(y)(Q_h(1) - Q_h(x)) & \text{for } x > y \end{cases}$$

where $Q_h(x) := \int_0^x (h(v))^{-2} \, \mathrm{d}v$. See Figure 11 Furthermore, in Appendix A we show that the kernel operator $K_h : \mathbb{L}_2([0,1]) \to \mathbb{H}_0^2([0,1])$

$$K_h f(x) = \int_0^1 k_h(x,y) f(y) \, \mathrm{d}y \tag{7.56}$$

is the right-inverse of the covariant Laplacian

$$(D^h)^* D^h K_h f = f \text{ for all } f \in \mathbb{L}_2([0,1]). \tag{7.57}$$

Now the operator norm of the bounded operator K_h can be estimated by the Hilbert-Schmidt norm

$$\|K_h\| \leq |||K_h||| = \sqrt{\mathrm{trace} K_h^* K_h} = \|k_h\|_{\mathbb{L}_2([0,1]\times[0,1])} \leq 2\|h^{-1}\|_{\mathbb{L}_2(0,1)} \|h\|_{\mathbb{L}_2(0,1)} \tag{7.58}$$

and as a result from (7.57) and (7.58) we find the following lower bound for the 1D-covariant Laplacian

$$(D^h)^* D^h \geq \frac{1}{|||K_h|||} \geq \tilde{c}_h([0,1]) \geq \frac{1}{2} \|h^{-1}\|_{\mathbb{L}_2(0,1)}^{-1} \|h\|_{\mathbb{L}_2(0,1)}^{-1} \ . \tag{7.59}$$

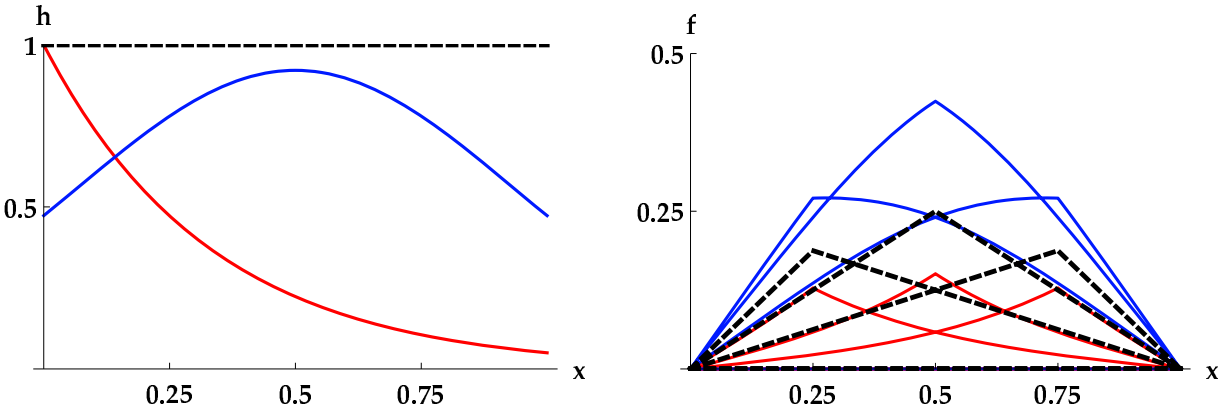

Figure 11: The graphs of gauge functions h and the corresponding Green's functions $k_h(\cdot, y)$ of the *covariant* Laplacian (where delta-spikes are respectively placed at $y = 0.25, 0.5, 0.75$). In red: gauge function of Example 1 (convex case, $\gamma = 3$). In blue: gauge function of Example 2 (concave case, $\sigma = \frac{1}{4}\sqrt{3}$). In dashed black: Green's function with respect to constant gauge functions (i.e. Green's function of standard Laplacian). The Green's function is convex (concave) if the gauge field is convex (concave) in accordance with Lemma A.4 in Appendix A.

So that Eq. (7.59) and Eq. (7.55) provide a general lower-bound $c_h([0,1] \times [0,1])$ for the the $2D$ case that explicitly depends on the gauge field

$$\begin{aligned} -\Delta + \tfrac{\Delta h}{h} \quad &> c_h([0,1] \times [0,1]) \\ &\geq \tfrac{1}{2} \min_{x \in [0,1]} \|h^{-1}(x,\cdot)\|_{\mathbb{L}_2(0,1)} \|h(x,\cdot)\|_{\mathbb{L}_2(0,1)} + \tfrac{1}{2} \min_{y \in [0,1]} \|h^{-1}(\cdot,y)\|_{\mathbb{L}_2(0,1)} \|h(\cdot,y)\|_{\mathbb{L}_2(0,1)} \ . \end{aligned} \tag{7.60}$$

Furthermore, we note that K_h is a compact operator due to (7.58), since every Hilbert Schmidt operator is compact, moreover both operator $(D^h)^* D^h$ (unbounded on $\mathbb{L}_2([0,1])$) and operator K_h are self-adjoint (with $k_h(x,y) = k(y,x)$) and by the spectral decomposition theorem for compact self-adjoint operators they share a common orthonormal basis of eigen functions. Consequently, the sharpest coercivity lower bound $\tilde{c}_h([0,1])$ coincides with the smallest eigenvalue of operator $(D^h)^* D^h$ and largest eigenvalue of operator K_h.

Finally, we note that the invariance of scaling the gauge function

$$(D^h)^* D^h = (D^{\lambda h})^* D^{\lambda h} \text{ and } K_h = K_{\lambda h} \text{ and } c_h = c_{\lambda h}, \quad , \lambda \neq 0,$$

is also reflected in the estimate (7.60).

8 The Euler-Lagrange equations for Tikhonov regularized optic flow reconstruction in covariant derivatives

In order to formulate Tikhonov regularization in covariant derivatives, we first have to derive a gauge field. Such a gauge field imposes an a priori balance between velocity magnitude and velocity field changes and thereby it is supposed to be close to the velocity field that we would like to reconstruct from a sparse set of features. There are several options to choose the gauge field as an initial guess for the velocity field. One could take the velocity field $\mathbf{v}^{k-1}$ of the previous time frame as a gauge field if one can assume that an a priori balance between velocity magnitude and velocity field changes is preserved over time. In the general setting however, it is better to use the standard Tikhonov regularization reconstruction with standard derivatives as a gauge field for the subsequent Tikhonov regularization reconstruction using covariant derivatives. The latter step is then to be considered as a refinement of the first.

In both two steps one needs the same algorithm as the standard Tikhonov regularization reconstruction with conventional derivatives coincides Tikhonov regularization reconstruction with covariant derivatives

using a constant gauge field. Summarizing, the velocity field at time-step $\mathbf{v}^k = \mathbf{v}^{k,1}\mathbf{e}_1 + \mathbf{v}^{k,2}\mathbf{e}_2$ is obtained by first minimizing

$$\begin{aligned}\mathcal{E}^{\lambda,\mathbf{h}^k,\mathbf{d}^k}(\mathbf{v}^k) &:= \lambda\mathcal{E}^{\mathbf{h}^k}_{reg}(\mathbf{v}^k) + \mathcal{E}^{\mathbf{d}^k}_{\text{data}}(\mathbf{v}^k) := \\ &\lambda \int_\Omega |||D^{\mathbf{h}^k}\mathbf{v}^k(\mathbf{x})|||^2 \,\mathrm{d}\mathbf{x} + \sum_{q=1}^{N_B}\sum_{j=1}^{2} w_q^k\, |(\phi_k^q, v^{k,j})_{\mathbb{L}_2(\Omega)} - d_q^{k,j}|^2\end{aligned} \tag{8.61}$$

for $\mathbf{h}^k = (1,1)$ yielding optimal field say $(\mathbf{v}^k)^*$ which produces the gauge field $\mathbf{h}^k := (\mathbf{v}^k)^*$ for the final step where again (8.61) is minimized (but now with a non-constant gauge field $\mathbf{h}^k := (\mathbf{v}^k)^*$). The parameter $\lambda > 0$ balances between regularization part (prior term) and the soft constraints (data term).

Firstly, we note that the soft constraints are due to

$$(\phi_k^q, v^{k,j})_{\mathbb{L}_2(\Omega)} = (\phi_{s_q} * v^{kj})(\mathbf{x}_q) = d_q^{k,j}, \tag{8.62}$$

where k indexes time, q enumerates the extremal branches, $j \in \{1,2\}$ enumerates the vertical and horizontal component of the field,

$$\phi_k^q(\mathbf{x}) := \phi_{s_q}(\mathbf{x} - \mathbf{x}_q) \tag{8.63}$$

denotes the Gaussian kernel (3.2) centered around $\mathbf{x}_q$ with scale $s_q > 0$, recall Figure 4 and where the sparse velocity components $d_q^{k,j}$, Eq. (4.8), are derived by solving Eq. (4.7). Too simplify our notation in the sequel we shall write

$$\begin{aligned}&\mathbf{d}^k := (\mathbf{d}^{k,1}, \mathbf{d}^{k,2})^T \\ &\mathbf{d}^{k,j} := (d_1^{k,j}, d_2^{k,j}, \ldots, d_{N_B}^{k,j})^T \in \mathbb{R}^{N_B}.\end{aligned} \tag{8.64}$$

Secondly, we note that $|||D^{\mathbf{h}^k}\mathbf{v}^k(\mathbf{x})|||$ in (8.61) denotes the Hilbert-Schmidt norm of the tensor field $D^{\mathbf{h}^k}\mathbf{v}^k(\mathbf{x}) = \sum_{i,j=1}^2 \partial_{x^i}^{h^{k,j}} v^{k,j}(\mathbf{x})\,\mathrm{d}x^i \otimes \partial_j$, i.e.:

$$|||D^{\mathbf{h}^k}\mathbf{v}^k(\mathbf{x})|||^2 = \sum_{i=1}^{2}\sum_{j=1}^{2} |\partial_{x^i}^{h^{k,j}} v^{k,j}(\mathbf{x})|^2 \ .$$

Finally, we note that for $\lambda = 0$ (and hard-constraints, i.e. $w_q^k \to \infty$) the minimizer is obtained by $\mathbb{L}_2$-projection, [9][ch:3.4], and for $\lambda > 0$ we arrive at the minimization framework on a space of Sobolev-type, [9][ch:3.4.2.1], where we must set $\mathcal{R} = (-(D^{\mathbf{h}^k})^* D^{\mathbf{h}^k} + I)^{\frac{1}{2}}$ to construct the complete Sobolev-space $\mathcal{D}(\mathcal{R}) = \{\mathbf{v} \in \mathbf{L}_2(\mathbb{R}^2) \mid \mathcal{R}f \in \mathbf{L}_2(\mathbb{R}^2)\}$ (depending on the gauge field) on which the minimization problem takes place.[6]

The Euler-Lagrange equations for the unique minimizer of (8.61) are derived by

$$\lim_{\epsilon\to 0} \frac{\mathcal{E}^{\lambda,\mathbf{h}^k,\mathbf{d}^k}(\mathbf{v}^k + \epsilon\boldsymbol{\delta}) - \mathcal{E}^{\lambda,\mathbf{h}^k,\mathbf{d}^k}(\mathbf{v}^k)}{\epsilon} = 0$$

which is supposed to hold for all infinitely smooth perturbations that are compactly within the interior of Ω, i.e. $\boldsymbol{\delta} \in \mathcal{D}(\Omega)$. Now straightforward computations in the general continuous Tikhonov regularization framework yield

$$\boxed{\begin{aligned}&\forall_{\boldsymbol{\delta}\in\mathcal{D}(\Omega)}\ 2\left((-\lambda\,(D^{\mathbf{h}^k})^* D^{\mathbf{h}^k})\mathbf{v}^k + \mathcal{S}_k^*\Lambda_k\mathcal{S}_k\mathbf{v}^k - \mathcal{S}_k^*\mathbf{d}^k, \boldsymbol{\delta}\right) = 0 \\ &\qquad\qquad \Leftrightarrow \\ &(-\lambda\,(D^{\mathbf{h}^k})^* D^{\mathbf{h}^k} + \mathcal{S}_k^*\Lambda_k\mathcal{S}_k)\mathbf{v}^k = \mathcal{S}_k^*\Lambda_k\mathbf{d}^k\end{aligned}} \tag{8.65}$$

where $\mathcal{S}_k : \mathbf{L}_2(\Omega) \to \mathbb{R}^{2\times N_B}$ is given by

$$(\mathcal{S}_k\mathbf{v}^k)(q) = (\phi_k^q, \mathbf{v}^k) := (\phi_k^q, v^{k,1})_{\mathbb{L}_2(\Omega)}\mathbf{e}_1 + (\phi_k^q, v^{k,2})_{\mathbb{L}_2(\Omega)}\mathbf{e}_2.$$

[6] According to the general theory in [9] the minimization problem can be extended to the full space $\mathbb{L}_2(\mathbb{R}^2)$ by means of the Gelfand-triple $\mathcal{D}(\mathcal{R}) \hookrightarrow \mathbb{L}_2(\mathbb{R}^2) \hookrightarrow (\mathcal{D}(\mathcal{R}))^*$, but this is a minor technical issue.

and where $\Lambda_k \in \mathbb{R}^{N_B \times N_B}$ is the diagonal matrix consisting of the corresponding feature weights:

$$\Lambda_k = \mathrm{diag}\{(w_q^k)_{q=1}^{N_B}\}.$$

Recall that N_B denotes the number of features (the number of extremal branches in our scale space representation, recall (4.1)). Note that the adjoint $\mathcal{S}_k^* : \mathbb{R}^{2\times N_B} \to \mathbf{L}_2(\Omega)$ operator for each fixed discrete time $k \in \mathbb{N}$ is defined by

$$(\mathcal{S}_k^*\Phi, \mathbf{v}^k)_{\mathbf{L}_2(\Omega)} = (\Phi, \mathcal{S}_k\mathbf{v}^k)_{\mathbb{R}^{2\times N_B}} \ ,$$

or more explicitly by

$$\begin{aligned}\int_\Omega ((S_k^*\Phi)(\mathbf{x}))^1 v^{k,1}(\mathbf{x}) + ((S_k^*\Phi)(\mathbf{x}))^2 v^{k,2}(\mathbf{x})\,\mathrm{d}\mathbf{x} \ &= \sum_{j=1}^{2}\sum_{q=1}^{N_B} (\Phi(q))^j\,(\mathcal{S}_k\mathbf{v}^k(q))^j = \sum_{j=1}^{2}\sum_{q=1}^{N_B}(\phi_k^q, v^{k,j})(\Phi(q))^j \\ &= \int_\Omega \left(\sum_{j=1}^{N_B}\mathbf{e}_j\left(\sum_{q=1}^{N_B}(\Phi(q))^j\phi_k^q(\mathbf{x})\right)\right)\cdot\mathbf{v}^k(\mathbf{x})\mathrm{d}\mathbf{x}\end{aligned}$$

so that the adjoint is simply given by

$$(S_k^*\Phi)(\mathbf{x}) = \sum_{j=1}^{2}\mathbf{e}_j\left(\sum_{q=1}^{N_B}(\Phi(q))^j\phi_k^q(\mathbf{x})\right)$$

This allows to write down the Euler-Lagrange equations (8.65) in more explicit form:

$$\begin{aligned}&\sum_{q=1}^{N_B} w_q^k\,\left((\phi_k^q, v^{k,j})_{\mathbb{L}_2(\Omega)} - (d_q^k)^j\right)\phi_k^q(\mathbf{x}) \\ &\quad +\lambda\,\left(-\Delta|v^{k,j}|(\mathbf{x}) + \eta\tfrac{\Delta|h^{k,j}|(\mathbf{x})}{|h^{k,j}|(\mathbf{x})}v^{k,j}(\mathbf{x})\right) = 0\end{aligned} \tag{8.66}$$

for $j = 1, 2$, $\mathbf{x} \in \mathbb{R}^2$. Recall from Section 7.2.1 that we can interpolate between regular and covariant derivatives with the parameter η. We will use (8.66) as a starting point for our implementations where all field components are expanded in a B-spline basis. Nevertheless, the more structured abstract form (8.65) clearly reveals the relevance of a negative (semi)-definite covariant derivative and the addition of a $\mathbb{L}_2$-norm in the energy minimization. To this end we note that $\mathcal{S}_k^*\Lambda_k\mathcal{S}_k$ is bounded from below (see subsection 7.3) so that

$$((-\lambda\,(D^{\mathbf{h}^k})^*D^{\mathbf{h}^k} + \mathcal{S}_k^*\Lambda_k\mathcal{S}_k)\mathbf{v}, \mathbf{v})_{\mathbf{L}_2(\Omega)} > \mathbf{c}(\Omega)\,\lambda(\mathbf{v}, \mathbf{v})_{\mathbf{L}_2(\Omega)}$$

and thereby the operator $-\lambda\,(D^{\mathbf{h}^k})^*D^{\mathbf{h}^k} + \alpha\,I + \mathcal{S}_k^*\Lambda_k\mathcal{S}_k$ is invertible and we can write the unique stable solution of (8.61) as

$$\mathbf{v}^k = (-\lambda\,(D^{\mathbf{h}^k})^*D^{\mathbf{h}^k} + \mathcal{S}_k^*\Lambda_k\mathcal{S}_k)^{-1}\mathcal{S}_k^*\Lambda_k\,\mathbf{d}^k \ . \tag{8.67}$$

8.1 Algorithm: Solving the Euler-Lagrange Equations by Expansion in B-splines

Next we express the Euler-Lagrange equations entirely in B-spline coefficients. The computational advantages of using B-splines for variational approaches are well-known in signal in image processing, [48, 27, 15]. We will first provide a few basic properties on B-splines that we will need for our algorithm and the analysis of its stability later on.

The n-th order B-spline is given by $n-1$-fold convolution with B^0

$$B^n(x) = \left(B^0 *^{n-1} B^0\right)(x) \text{ with } B^0(x) = 1_{[-\frac{1}{2},\frac{1}{2}]}(x). \tag{8.68}$$

where $f*g(x) = \int_{-\infty}^{\infty} f(y)g(x-y)\mathrm{d}y$. Thereby the n-th order B-spline is compactly supported on $1_{[-\frac{n}{2}-\frac{1}{2},\frac{n}{2}+\frac{1}{2}]}$. In the discrete setting we sample on a uniform integer grid, so for example if n is odd we find n non-zero-samples. Next we provide a list of Z-transforms of B-splines sampled on a uniform grid with stepsize 1:

$$\begin{array}{l} ZB^2(z) = \frac{1}{2!2^2}(z^{-1}+3+z)\ , \\ ZB^3(z) = \frac{1}{3!}(z^{-1}+4+z)\ , \\ ZB^4(z) = \frac{1}{3!2^3}(z^{-2}+76z^{-1}+230+76z+z^2)\ , \\ ZB^5(z) = \frac{1}{5!}(z^{-2}+26z^{-1}+66+26z+z^2)\ , \\ ZB^6(z) = \frac{1}{6!2^6}(z^{-3}+722z^{-2}+10543z^{-1}+23548+10543z+722z^2+z^3). \end{array} \tag{8.69}$$

The regular derivative of a B-spline of order n is expressed in B-splines of order $n-1$

$$\frac{d}{dx}B^n(x) = B^{n-1}(x+1/2) - B^{n-1}(x-1/2)$$

and nicely matches the well-known a finite difference stencil. Consequently, for even order derivatives of B-splines we have

$$(B^n)^{(2k)}(x) = \sum_{l=-k}^{k}(-1)^l\binom{k}{|l|}B^{n-2k}(x-l)\ .$$

so for example for $2k=2$ we see $(B^n)^{(2)}(x) = B^{n-2}(x+1) - 2B^{n-2}(x) + B^{n-2}(x-1)$, which nicely matches the finite difference $[1,-2,1]$-stencil for a second order derivative.

Next we express the unknown velocities $v^{k,j} : \Omega \to \mathbb{R}$, $j = 1,2$, at time-frame $t = k\Delta t$, in periodic B-splines

$$v^{k,j}(x,y) = \sum_{l=0}^{L-1}\sum_{m=0}^{M-1} c_{lm}^{kj}\ B^n\left(\frac{x}{a} - m \mod \frac{M}{a}\right) B^n\left(\frac{y}{b} - l \mod \frac{L}{b}\right) \tag{8.70}$$

for all $(x,y) \in \Omega = [0,M]\times[0,L]$. In our algorithms we set the resolution parameters $a = b = 1$. One can choose them differently, like in [27], as long as the n-th B-spline is properly sampled on $[0,M]$ and $[0,L]$, i.e.

$$\frac{M}{a} > n+1 \text{ and } \frac{L}{b} > n+1\ . \tag{8.71}$$

Recall that we always ensure our velocity fields to vanish at the boundaries, since we first extract the Harmonic infilling:

$$\mathbf{v}^k \mapsto \mathbf{v}^k - \left(\mathbf{v}^k\big|_{\partial\Omega}\right)_{\mathcal{H}}$$

Recall (5.23), which allows us to use periodic B-splines. By property (8.68) and assuming (8.71) we have the following formula for the components of rank-2 tensor on $\mathbb{R}^P$:

$$\begin{array}{rl} T_{P,k}^{pp'} & := \frac{1}{a}\int_0^P (B^n)^{(k)}(\frac{x}{a} - p \mod \frac{P}{a})\ B^n(\frac{x}{a} - p' \mod \frac{P}{a})\ \mathrm{d}x \\ & = \frac{1}{a}\int_{-\frac{P}{2}}^{\frac{P}{2}} (B^n)^{(k)}(\frac{x}{a} - p \mod \frac{P}{a})\ B^n(\frac{x}{a} - p' \mod \frac{P}{a})\ \mathrm{d}x \\ & = (B^{2n})^{(k)}(p - p' \mod P)\ . \end{array}$$

with $P \in \{M, L\}$. Now after straightforward but intense computations one can rewrite the energy (8.61) as

$$\begin{array}{l} \mathcal{E}_{\lambda,\alpha,\mathbf{h}^k,\mathbf{d}^k}(\mathbf{v}^k, \mathbf{v}^{k-1}, \mathbf{d}^k) = E_{\lambda,\mathbf{h}^k,\mathbf{d}^k}(\mathbf{c}^k, \mathbf{d}^k) := \\ \sum_{j=1}^{2}(\mathbf{c}^{kj}, R_{k,j}^{\lambda}\mathbf{c}^{kj})_{\ell_2(\{1,\ldots,LM\})} + \|\Lambda_k^{1/2}(S\mathbf{c}^{k,j} - \mathbf{d}^{k,j})\|^2_{\ell_2(\{1,\ldots,N_B\})} \end{array} \tag{8.72}$$

with

$$\begin{array}{rl} \mathbf{c}^k & = ((\mathbf{c}^{k,1})^T, (\mathbf{c}^{k,2})^T)^T = \Big(c_{11}^{k,1}, c_{12}^{k,1}, \ldots, c_{1M}^{k,1}, c_{21}^{k,1}, c_{22}^{k,1}, \ldots, c_{2M}^{k,1}, \ldots, \ldots, c_{L1}^{k,1}, c_{L2}^{k,1}, \ldots, c_{LM}^{k,1}\ ; \\ & (c_{11}^{k,2}, c_{12}^{k,2}, \ldots, c_{1M}^{k,2}, c_{21}^{k,2}, c_{22}^{k,2}, \ldots, c_{2M}^{k,2}, \ldots, \ldots, c_{L1}^{k,2}, c_{L2}^{k,2}, \ldots, c_{LM}^{k,2}\Big)^T \in \mathbb{R}^{2M*L} \end{array} \tag{8.73}$$

and where the matrix representation of the covariant Laplacian expressed in the B-spline basis is given by

$$R^{\lambda}_{k,j} \quad = \lambda(-T_{L,0}(\tfrac{y}{b}) \otimes T_{M,2}(\tfrac{x}{a}) - T_{L,2}(\tfrac{y}{b}) \otimes T_{M,0}(\tfrac{x}{a}) + \lambda \sum_{x=0}^{M-1} \sum_{y=0}^{L-1} \gamma^j_k(x,y)(\tilde{T}_{L,0}(\tfrac{y}{b}) \otimes \tilde{T}_{M,0}(\tfrac{x}{a})) \quad (8.74)$$

where

$$(\mathbf{c}^{k,j}, R_{L,0} \otimes R_{M,0}\mathbf{c}^{k,j}) = \sum_{l,l'=0}^{L-1} \sum_{m,m'}^{M-1} c^{k,j}_{lm} c^{k,j}_{l'm'} (R_{L,0})_{ll'} (R_{M,0})_{mm'}$$

and $A \otimes B$ denotes the Kronecker product of matrices (related to the tensor product of the corresponding tensors) and where

$$\tilde{T}_{P,k}(u) = [(\tilde{T}_{P,k}(u)]_{pp'} = (B^n)^{(k)}(u-p)B^n(u-p')$$

with $p, p' \in \{1, \ldots, P\}$ (note that we either set $P = M$ and $p = m$, $p = m'$ or $P = L$ and $p = l$, $p = l'$ in (8.74)) and where the

$$\gamma^{k,j}(x,y) = \frac{\Delta h^{k,j}(x,y)}{h^{k,j}(x,y)} = -\Delta(-\log|h^{k,j} + \delta|)(x,y) + \|\nabla \log|h^{k,j} + \delta|(x,y)\|^2 \ ,$$

is dimensionless and where $1 \gg>> \delta > 0$ is added to the gauge field to avoid singularities.

The mapping $\mathcal{S}$ in (8.65) expressed in B-spline coefficients $\mathbf{c}^k$ is given by

$$\mathcal{S}\mathbf{c}^k(q) = \sum_{j=1}^{2} \mathbf{e}_j \left(\sum_{l=0}^{L-1} \sum_{m=0}^{M-1} c^{k,j}_{lm} \ \left(\phi^q_k \ , \ B^n\left(\frac{\cdot}{a} - m + \mathrm{Mod}(M)\right) B^n\left(\frac{\cdot}{b} - l + \mathrm{Mod}(L)\right)\right)\right)$$

If we expand the feature vectors $\{\phi^q_k\}_{q=1}^{N_B}$ as well

$$\phi^q_k = \sum_{m'=1}^{M-1} \sum_{l'=0}^{L-1} \tilde{c}^{k,q}_{l'm'} B^n\left(\frac{\cdot}{a} - m' \ \mathrm{Mod}(M)\right) B^n\left(\frac{\cdot}{b} - l' \ \mathrm{Mod}(L)\right),$$

then we may rewrite the mapping $\mathcal{S} : \mathbb{R}^{2LM} \to \mathbb{R}^q$ as

$$\mathcal{S}\mathbf{c}^k(q) \quad = \sum_{l,l'=0}^{L-1} \sum_{m,m'=0}^{M-1} \tilde{c}^{kq}_{lm'} T^{mm'}_{M,0} T^{ll'}_{L,0} c^{kj}_{lm} = (\tilde{\mathbf{c}}^{kq})^T (T_{L,0} \otimes T_{M,0})\, \mathbf{c}^{kj}$$

In order to derive the minimizer of the discrete functional (8.72) which coincides with the minimizer of the continuous functional (8.65), (8.67) if we restrict ourselves to velocities $\mathbf{v}^k$ which are within the (closed) subspace $\mathrm{span}_{m=0,\ldots,M-1,l=0,\ldots,L-1}\{B^n\left(\frac{\cdot}{a} - m \ \mathrm{Mod}(M)\right) B^n\left(\frac{\cdot}{b} - l \ \mathrm{Mod}(L)\right)\}$, we simply set

$$\nabla_{\mathbf{c}^k} E_{\lambda,h^k,d^k}(\mathbf{c}^k) = \mathbf{0} \ ,$$

which yields (expressed in the natural matrix-representation $S \in \mathbb{R}^{N_B \times LM}$ of the isomorphic mappings $\mathbf{c}^{k1} \mapsto \mathcal{S}(\mathbf{c}^{k1}, \mathbf{0})$ and $\mathbf{c}^{k2} \mapsto \mathcal{S}(\mathbf{0}, \mathbf{c}^{k2})$)

$$(R^{\lambda}_k + S^T \Lambda_k S)\mathbf{c}^{k,j} = S^T \Lambda_k \mathbf{d}^{k,j} \text{ for } j = 1, 2,$$

with $\mathbf{d}^{k,j}$ given by (8.64) Now for $n \leq 3$ we find (akin to (8.67)) the unique solution by inversion

$$\mathbf{c}^{k,j} = (R^{\lambda}_{k,j} + S^T \Lambda_k S)^{-1} S^T \Lambda_k \mathbf{d}^{k,j} \ , \quad (8.75)$$

which we solved by a BiCSTAB algorithm (Conjugate gradient is not suitable since the matrix R^{λ}_k is not symmetric due to the fact that the adjoint of a covariant derivative is not equal to minus the covariant derivative, recall (7.48)). Here we have exploited the direct product structure of the terms in the matrix R^{λ}_k (8.74): For numerical efficiency one only needs to store the product $M \times M$ or $L \times L$ matrices such as $T_{M,0}$ and $T_{L,0}$ using the computation scheme explained in [22] in the BiCSTAB algorithm whenever a matrix product occurs.

8.1.1 Stability Analysis of the Linear System in the Euler Lagrange Equations

In this paragraph we will analyse the stability of the inversion scheme (8.75) which is basically the matrix representation of operator equation (8.67). In the latter case the theoretic continuous operator

$$-\lambda\,(D^{\mathbf{h}^k})^* D^{\mathbf{h}^k} + \mathcal{S}_k^* \Lambda_k \mathcal{S}_k \tag{8.76}$$

can be inverted in (8.67) since by our results in Section 7.3 (and the Lax-Milgram theorem [37]) we have

$$-\lambda\,(D^{\mathbf{h}^k})^* D^{\mathbf{h}^k} \geq \lambda\, c_{\mathbf{h}^k} \text{ and}$$
$$\mathcal{S}_k^* \Lambda_k \mathcal{S}_k \geq 0\ ,$$

where $c_{\mathbf{h}^k}$ is the Poincar'e constant of the covariant Laplacian, which depends on the choice of gauge field $\mathbf{h}^k$, which can be slightly smaller than the Poincar'e constant of regular Laplacian in specially designed examples where the gauge field is (nearly) everywhere concave such as in Example 2, but which is in practice (where gauge fields are mainly convex in Ω) larger than the Poincaré constant of the regular Laplacian. On a rectangle $\Omega = [0, M] \times [0, L]$ this means $c_{\mathbf{h}^k} \geq \pi^2(M^{-2} + L^{-2})$. In the remainder of this section we shall assume that $c_{\mathbf{h}^k}$ is given. For lower bounds on $c_{\mathbf{h}^k}$ see Appendix A.

Let us return to the finite matrix representations $R^\lambda_{k,j} + S^T \Lambda_k S$, $j = 1, 2$ of operator (8.76) with respect to the periodic B-spline basis (8.70). We would like to get estimates for the smallest eigen value of this finite matrix and we would like to investigate how this smallest eigenvalue depends on the order of the B-splines.

First of all we observe that the data matrix $S^T \Lambda_k S$ is only positive *semi*-definite. The problem is that the matrix representation of S is of size $\mathbb{R}^{N_B \times LM}$, where in general we have a sparse set of features, i.e. $LM >> N_B$, i.e. even in the case where all features are linearly dependent S has a lot of linear dependence in its columns, i.e. S is not injective, $\mathcal{S}$ has a very large nil-space and $S^T \Lambda_k S$ is not invertible. So we should not expect global stability from the data-matrix. However, the smoothness matrix $R^\lambda_{k,j}$ for each component $j \in \{0, 1\}$ satisfies

$$R^\lambda_{k,j} \geq c_{\mathbf{h}^k}\ \lambda\, T_{L,0} \otimes T_{M,0} \tag{8.77}$$

since substitution of (8.70) into $(\mathbf{v}, \mathbf{v})_{\mathbb{L}_2(\Omega)}$, $\Omega = [0, M] \times [0, L]$, gives

$$\sum_{j=1}^{2} (\mathbf{c}^{kj}, R^\lambda_{k,j} \mathbf{c}^{kj})_{\ell_2(\{1,\ldots,LM\})} = (-\lambda\,(D^{\mathbf{h}^k})^* D^{\mathbf{h}^k} \mathbf{v}, \mathbf{v})_{\mathbb{L}_2(\Omega)} \geq$$
$$c_{\mathbf{h}^k} (\mathbf{v}, \mathbf{v})_{\mathbb{L}_2(\Omega)} = c_{\mathbf{h}^k}\ \lambda \sum_{j=1}^{2} (\mathbf{c}^{kj}, T_{L,0} \otimes T_{M,0} \mathbf{c}^{kj})_{\ell_2(\{1,\ldots,LM\})}\ .$$

Now (8.77) relates the stability of matrix $T_{L,0} \otimes T_{M,0}$ with inverse $(T_{L,0} \otimes T_{M,0})^{-1} = T_{L,0}^{-1} \otimes T_{M,0}^{-1}$ to the stability of $R^{\lambda_{k,j}}$. Now the eigenvalues of $T_{L,0} \otimes T_{M,0}$ are direct products of the eigenvalues of $T_{L,0}$ with the eigenvalues of $T_{M,0}$ so in order to find a lower-bound of the smallest eigenvalue of $R^\lambda_{k,j}$ we derive the smallest eigenvalue of $T_{P,0}$ with $P \in \{M, L\}$. Now $T_{P,0} = [T_{P,0}]_{pp'} = [B^{2n}(p - p' \text{ Mod } P)]_{pp'}$ is a *circulant Toeplitz matrix* whose columns add up to one. This matrix is not symmetric (due to periodicity) so its eigen values need not be real-valued. It is positive definite though and since

$$(\mathbf{c}^{kj}, T_{L,0} \otimes T_{M,0} \mathbf{c}^{kj})_{\ell_2(\{1,\ldots,LM\})} = (\mathbf{c}^{kj}, \frac{1}{2}(T_{L,0} \otimes T_{M,0} + (T_{L,0} \otimes T_{M,0})^T) + \mathbf{c}^{kj})_{\ell_2(\{1,\ldots,LM\})}\ ,$$

we are only interested in the real part of the eigenvalues $\text{Re}(\lambda) = \frac{1}{2}(\lambda + \overline{\lambda})$. The Gerschgorin circle theorem [18] shows that the eigenvalues are contained within the circles

$$|\lambda - B^{2n}(0)| \leq 1 - B^{2n}(0) \Leftrightarrow \sqrt{|\text{Re}(\lambda) - B^{2n}(0)|^2 + |\text{Im}(\lambda)|^2} \leq 1 - B^{2n}(0)\ , \tag{8.78}$$

where we note that $2B^{2n}(0) - 1$ is strictly positive iff $n \leq 3$. In fact $n = 3$ yields $B^6(0) = \frac{2 35486!}{2^6} = \frac{5887}{11520} \approx 0.511$ which is already close to a half. The eigenvalues and eigenvectors of circulant Toeplitz matrices can

be computed explicitly, in fact it is well-known that the eigenvalues of a circulant Toeplitz matrix coincide with the Discrete Fourier Transform (DFT) of the first row of such a matrix:

$$\begin{aligned}\lambda_p &= \sum_{p'=0}^{P-1} B^{2n}(p') e^{\frac{-2\pi p' pi}{P}} \ , \\ \mathrm{Re}(\lambda_p) &= \tfrac{1}{2}\sum_{p'=0}^{P-1} B^{2n}(p') e^{\frac{-2\pi p' pi}{P}} + \tfrac{1}{2}\sum_{p'=0}^{P-1} B^{2n}(p') e^{\frac{+2\pi p' pi}{P}} \\ &= \tfrac{1}{2}B^{2n}(0) + \tfrac{1}{2}(ZB^{2n})(e^{\frac{-2\pi pi}{P}}) \ ,\end{aligned} \tag{8.79}$$

with corresponding eigenvector $(1, e^{-\frac{2\pi ip}{P}}, e^{-\frac{2\pi ip(P-1)}{P}})^T \in \mathbb{R}^P$, $p = 0, \ldots, P-1$. Here our list of Z-transforms of B-splines (8.69) comes at hand. Within the list one finds that

$$(ZB^{2n})(z) = \sum_{p'=-n}^{n} c_{p'}^{2n} z^{-p'} \ ,$$

with $c_{p'}^{2n} \in \mathbb{R}^+$ monotonically decreasing with $c_0^{2n} = B^{2n}(0)$ and therefore

$$B^{2n}(0) + \sum_{p'=1}^{P-1}(-1)^{p'} c_{p'}^{2n} = \mathrm{Re}(\lambda_{p=P/2}) \leq \mathrm{Re}(\lambda_p) = B^{2n}(0) + \sum_{p'=1}^{P-1} c_{p'}^{2n} \cos\left(\frac{2\pi pp'}{P}\right) \leq \mathrm{Re}(\lambda_0) = 1 \ ,$$

so that the minimal real part of the eigenvalues equals

$$\min_{p=0,\ldots,P-1}\{\Re(\lambda_p)\} = B^{2n}(0) + \sum_{p'=1}^{P-1}(-1)^{p'} c_{p'}^{2n} = \sum_{p'=0}^{P-1}(-1)^{p'} c_{p'}^{2n} > 0 \ .$$

Now clearly this minimal real part depends on the order of the B-splines n. Exact computations for $n \leq 10$ indicate that it is monotonically decreasing with n with values (rounded off in 3 digits) 0.625, 0.404, 0.298, 0.244, 0.212, 0.192, 0.178, 0.167, 0.157, 0.150 for respectively $n = 1, \ldots, 10$. So for example in our algorithms we set $n = 3$ and we obtain

$$R_{k,j}^{\lambda} \geq c_{\mathbf{h}^k}\ \lambda\ (0.2977)^2 \ ,$$

with $c_{\mathbf{h}^k} \gg \pi^2(M^{-2} + L^{-2}) \approx 0.0023$, with $M = L = 93$ and $\lambda = 10^{0.06} \approx 1.15$ (these parameter settings produced good results in our application in the experimental section, Section 10) which shows that the real part of the smallest eigenvalue of the matrix we inverted stays sufficiently far from 0. Hence we have established a theoretical underpinning of the stability of our algorithm (8.75) where we included the efficient Kronecker product computation scheme explained in [22] in the BiCSTAB algorithm to invert the matrix.

8.2 Rotation covariance

Clearly our algorithm commutes with translations, i.e. translation of input image $f : \mathbb{R}^2 \times \mathbb{R}^+ \to \mathbb{R}$ results in a translated optical flow vector field $\mathbf{v}$. With respect to rotations this commutation property is not a priori satisfied as we will show next. Subsequently, we explain why this violation is hardly visible in practice and we also show how to formally adapt the energy to obtain a fully rotation covariant algorithm.

Rotation of the input scalar field is given by $f \mapsto f_R$ whereas rotation of the output optic flow vector field is given by $\mathbf{v}^k \mapsto \mathbf{v}_R^k$, $k = 1, \ldots, K$, where

$$f_R(\mathbf{x}, t) = f(R^{-1}\mathbf{x}, t) \text{ and } \mathbf{v}_R(\mathbf{x}, t) = R\,\mathbf{v}(R^{-1}\mathbf{x}, t) \ .$$

Note that rotation covariance of the algorithm would follow by rotation invariance of the mappings $(\mathbf{v}^k, \mathbf{h}^k, \mathbf{d}^k) \mapsto \mathcal{E}^{\lambda,\mathbf{h}^k,\mathbf{d}^k}(\mathbf{v}^k)$, $k \in \mathbb{Z}$, i.e.

$$\mathcal{E}^{\lambda,\mathbf{h}_R^k,(R\mathbf{d}_q^k)_{q=1}^{N_B}}(\mathbf{v}_R^k) = \mathcal{E}^{\lambda,\mathbf{h}^k,(\mathbf{d}_q^k)_{q=1}^{N_B}}(\mathbf{v}^k) \tag{8.80}$$

for all $R \in SO(2)$, $k = 1, \ldots, K$. But the problem is that (8.80) is formally only a priori satisfied if R is a rotation over $n\pi/2$, with $n \in \mathbb{Z}$ as will show next.

Rotation of the input dynamic image f yields a rotated data vector $\mathbf{d}_k^q \mapsto R\mathbf{d}_k^q$ and

$$\mathcal{E}_{\text{data}}^{(R\mathbf{d}_k^q)_{q=1}^{N_B}}(\mathbf{v}_R) = \mathcal{E}_{\text{data}}^{(\mathbf{d}_k^q)_{q=1}^{N_B}}(\mathbf{v})$$

for all planar rotations $R \in SO(2)$. So the data-term is rotation invariant, but the regularization term satisfies

$$\begin{aligned}
\mathcal{E}^{\mathbf{h}_R^k}(\mathbf{v}_R^k) &= \textstyle\int_\Omega |||D^{\mathbf{h}^R}\mathbf{v}_R(\mathbf{x})|||^2 \,\mathrm{d}\mathbf{x} = \int_\Omega \sum_{i,j=1}^2 |\partial_{x^i}^{h_R^{k,j}} v_R^{k,j}(\mathbf{x})|^2 \,\mathrm{d}\mathbf{x} \\
&= \int_\Omega \sum_{i,j=1}^2 \left| \sum_{i',j'=1}^2 (R^{-1})_{i'}^i R_{j'}^j \left(\partial_{y^{i'}} v^{k,j'}(\mathbf{y}) - v^{k,j'}(\mathbf{y}) \partial_{y^{i'}} \log |\sum_{l'} R_{l'}^j h^{k,l'}(\mathbf{y})| \right) \right|^2 \mathrm{d}\mathbf{y} \\
&= \int_\Omega \sum_{i,j=1}^2 \left| \partial_{y^i} v^{k,j}(\mathbf{y}) - v^{k,j}(\mathbf{y}) \partial_{y^i} \log |\sum_{l'} R_{l'}^j h^{k,l'}(\mathbf{y})| \right|^2 \mathrm{d}\mathbf{y} \ ,
\end{aligned}$$

with $\mathbf{y} = R^{-1}\mathbf{x}$. Now it is easily verified that (8.80) is satisfied if R is a rotation over $n\pi/2$, where we recall (7.45). For the other cases it depends on the spherical fluctuations between on the fraction of slope and hight of the graph of the projected gauge field and the fraction of slope and hight of the graph of the projected velocity field, where projections take place on each orientation $\mathbf{n} \in S^2$.

In principle one can obtain strict rotation covariance by using the following regularization term of the energy instead

$$\tilde{\mathcal{E}}_{reg}^{\mathbf{h}^k}(\mathbf{v}^k) = \int_0^{2\pi} \|D^{\mathbf{h}^k(\mathbf{x})\cdot\mathbf{n}(\theta)}(\mathbf{v}^k(\mathbf{x})\cdot\mathbf{n}(\theta))\|^2 \,\mathrm{d}\theta \ , \tag{8.81}$$

with $\mathbf{n}(\theta) = (\cos\theta, \sin\theta)^T$. Note that $\mathcal{E}_{reg}^{\mathbf{h}^k}(\mathbf{v}^k)$ is a course sampling of $\tilde{\mathcal{E}}_{reg}^{\mathbf{h}^k}(\mathbf{v}^k)$ (sampled at $\{0, \frac{\pi}{2}, \pi, \frac{3\pi}{2}\}$), one may improve rotation invariance by including the orientation angles $\{\frac{\pi}{4}, \frac{3\pi}{4}\}$ as well. This is included in the algorithm by means of the replacement:

$$\begin{aligned}
&(D^{\mathbf{h}^k})^* D^{\mathbf{h}^k}\mathbf{v}^k(\mathbf{x}) = \sum_{i,j=1}^2 \left(\left(\tfrac{\partial}{\partial x^i}\right)^{h^{k,j}} \right)^* \left(\tfrac{\partial}{\partial x^i}\right)^{h^{k,j}} v^{k,j}(\mathbf{x})\,\mathbf{e}_j = \\
&\qquad\qquad \rightarrow \\
&\int_0^{2\pi} \sum_{i=1}^2 ((D^{h_\theta^k})^* D^{h_\theta^k} v_\theta^k)(\mathbf{x})\ \mathbf{n}(\theta)\,\mathrm{d}\theta = \int_0^{2\pi} (-\Delta v_\theta^k(\mathbf{x}) + \tfrac{\Delta h_\theta^k(\mathbf{x})}{h_\theta^k(\mathbf{x})}\, v_\theta^k(\mathbf{x}))\ \mathbf{n}(\theta)\,\mathrm{d}\theta
\end{aligned} \tag{8.82}$$

where we applied short notation $v_\theta^k := \mathbf{v}^k \cdot \mathbf{n}(\theta)$ and $h_\theta^k := \mathbf{h}^k \cdot \mathbf{n}(\theta)$.

At this point we recall Remark 7.3: For properly defined 2-tensors t on a circle one has $\int_0^{2\pi} t(\mathbf{n}(\theta), \mathbf{n}(\theta))\,\mathrm{d}\theta = \sum_{k\in\{0,1\}} t(\mathbf{n}(k\frac{\pi}{2}), \mathbf{n}(k\frac{\pi}{2})) = \text{trace}(t)$. In order to show that (8.81) has a minor correcting effect so that (8.82) is not needed in our applications, we show two typical experiments. We apply the proposed algorithm to a sequence presenting horizontal translation and to its rotate version (45 degrees); then we rotate the output of the horizontal translating sequence of 45 degrees and finally we compare the outcome of both sequences (cf. first two rows in Figure (12)). We applied a similar experiment but now to a real sequence of the contracting heart, where we rotated over 20 degrees. Again we see that the second column is visually close to the third column which coincides with our practical observation that the more expensive fully rotation covariant option (8.81) with corresponding replacement (8.82) is not really necessary.

Finally, we note that none of our experiments in section 10 show a bias towards the horizontal and vertical axis, despite the fact that we used $\mathcal{E}_{reg}^{\mathbf{h}^k}(\mathbf{v}^k)$, Eq. (8.61), rather than $\tilde{\mathcal{E}}_{reg}^{\mathbf{h}^k}(\mathbf{v}^k)$, Eq. (8.81).

9 The Euler-Lagrange equations of Tikhonov regularization in covariant derivatives using multi-scale Helmholtz decomposition

So far we have considered the multi-scale Helmholtz decomposition and the flow field reconstruction (or rather interpolation) based on Tikhonov regularizations using covariant derivatives. These two techniques

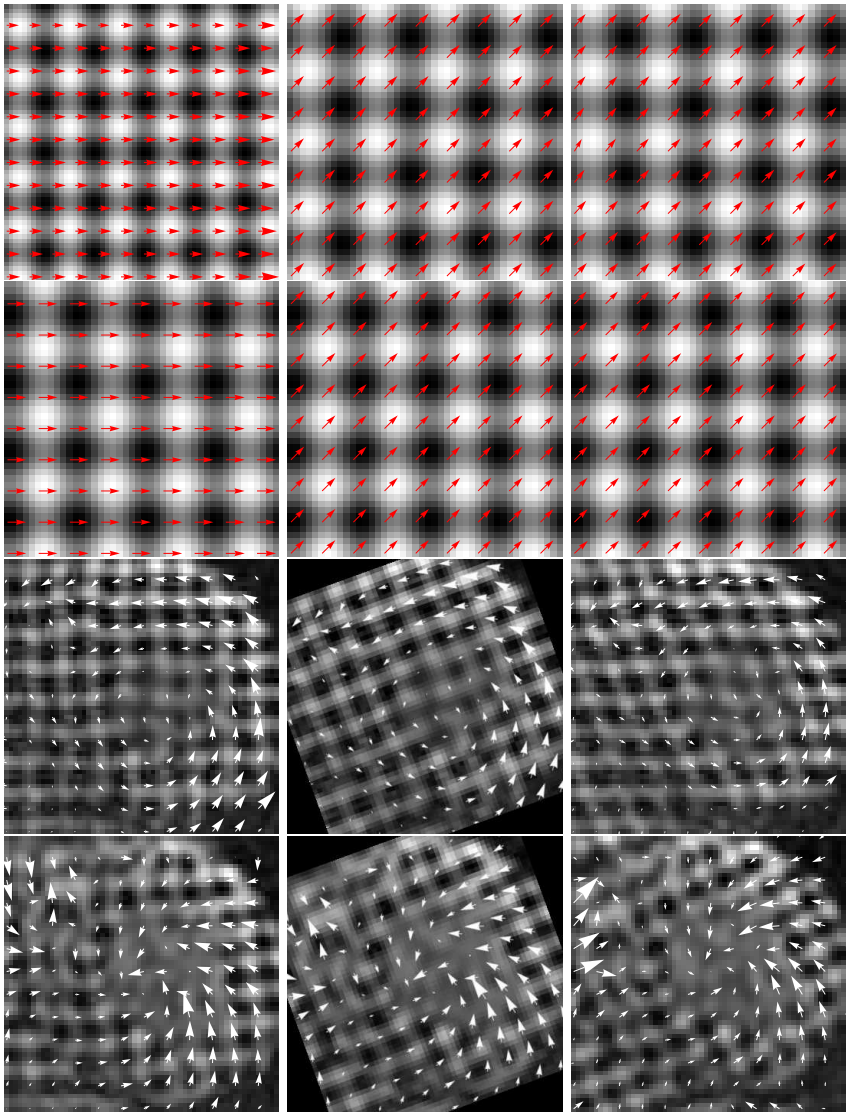

Figure 12: Rotation Covariance. We show two experiments displaying the output of the proposed algorithm for a translating sequence, displaying two time-frames $t = 3$ and $t = 6$ (top two rows) and for a cardiac image sequence, (bottom two rows). The first column shows the output $\mathbf{v}(x, y, t) = (\mathbf{v}(f))(x, y, t)$ depicted on top of the original input dynamic image $f(x, y, t)$, the second column shows the rotated output of the original input image i.e. $R(\mathbf{v}(f))(R^{-1}\mathbf{x}, t)$ is depicted on top of $f_R(\mathbf{x}, t) = f(R^{-1}\mathbf{x}, t)$, where R is the counterclockwise rotation over 45° resp. 20° degrees (using linear interpolation). The third column shows the output $(\mathbf{v}(f_R))(x, y, t)$ depicted on top of the input dynamic image $f_R(x, y, t)$.

are combined in our complete scheme depicted in Figure 1.

Although the scheme in Figure 1 produces good results in practice (as we will see in Section 10) it is remarkable that the output in the dense motion field reconstruction in Figure 1 is a sum of two Euler Lagrange optimizations separately performed on the rotation and divergence free part. To this end we also decompose the boundary conditions (8.62) ("sparse velocities") over the divergence and rotation free part as follows: We apply a reconstruction by means of a Tikhonov regularization scheme with standard derivatives and very small $0 < \lambda \ll 1$ to obtain a (full) regularized velocity field that (nearly) satisfies the hard constraints (as $0 < \lambda \ll 1$). Then we apply a Helmholtz decomposition on this field (with small scale) and from the Helmholtz decomposition we obtain the divergence free part and rotation free part vector at

the position of interest $\mathbf{x}_q$. In the sequel we shall denote these vectors as follows

$$\mathbf{d}^{k,j} = \mathbf{d}^{k,j,\mathrm{rf}} + \mathbf{d}^{k,j,\mathrm{df}} \tag{9.83}$$

where the label 'df' stands for divfree and the label 'rf' stands for rotfree. Note that (9.83) corresponds to the right green box "Helmholtz Decomposition of Sparse velocities" in Figure 1. Furthermore, the red boxes in Figure 1 correspond to minizing the energy (8.61) by means of Eq. (8.65) or more precisely by its dicrete version, Eq. (8.75), obtained by expressing Eq. (8.65) in a B-spline basis. Finally, we recall that the middle blue box is explained in Sections 3 and 4 yielding feature values $d^{k,j;q}$ and feature vectors ϕ_k^q, recall (8.62) and (8.63).

9.1 Towards a single Euler Lagrange system involving covariant derivatives and Helmholtz decomposition

In this subsection we will consider a *single* Euler-Lagrange system involving both multi-scale Helmholtz decomposition and covariant derivatives. We will see direct analogy with our approach in Figure 1. However, serious technical issues arise when trying to solve the single Euler-Lagrange system, due to the fact that Helmholtz decomposition is expressed in standard derivatives, whereas the energies we would like to minimize are expressed in covariant derivatives.

At a given fixed time frame $t = k\Delta t$ we minimize the following positive functional one

$$\begin{aligned}\mathcal{E}^{\lambda,\mathbf{h}^k,\mathbf{d}^k}(\mathbf{v}^k) \quad &:= \int_\Omega \lambda \,|||D^{(\mathbf{h}^k)^{\mathrm{divfree}}}\mathbf{v}^{k,\mathrm{divfree}}(\mathbf{x})|||^2 \,\mathrm{d}\mathbf{x} + \\ &\quad \int_\Omega \lambda \,|||D^{(\mathbf{h}^k)^{\mathrm{rotfree}}}\mathbf{v}^{k,\mathrm{rotfree}}(\mathbf{x})|||^2 \,\mathrm{d}\mathbf{x} \\ &\quad + \sum_{q=1}^{N_B} w_q^k \sum_{j=1}^{2} |(\phi_k^q, v^{k,j})_{\mathbb{L}_2(\Omega)} - d_q^{k,j}|^2\end{aligned} \tag{9.84}$$

where again $|||\cdot|||$ denotes the Hilbert-Schmidt norm and where we again first consider the simple case $\mathbf{h}_k = (1,1)^T$ (where all covariant derivatives become standard derivatives) yielding a unique solution that we set as our gauge field $\mathbf{h}^k$. So from now on we assume $\mathbf{h}^k$ is given. Then setting the first order variation of the energy given by Eq. (9.84) with respect to arbitrary smooth perturbation $\boldsymbol{\delta} \in (\mathcal{D}(\Omega))^2$ yields

$$\Big(-\lambda(D^{\mathbf{h}^{k,\mathrm{rf}}})^* D^{\mathbf{h}^{k,\mathrm{rf}}}\mathbf{v}^{k,\mathrm{rf}} - \lambda(D^{\mathbf{h}^{k,\mathrm{df}}})^* D^{\mathbf{h}^{k,\mathrm{df}}}\mathbf{v}^{k,\mathrm{df}} + \mathcal{S}_k^*\Lambda_k\mathcal{S}_k(\mathbf{v}^{k,\mathrm{rf}} + \mathbf{v}^{k,\mathrm{df}}) + \mathcal{S}_k^*(\mathbf{d}^{k,j,\mathrm{rf}} + \mathbf{d}^{k,j,\mathrm{rf}}), \boldsymbol{\delta}^{\mathrm{df}} + \boldsymbol{\delta}^{\mathrm{rf}}\Big) = 0. \tag{9.85}$$

where the label 'df' stands for divergence free and the label 'rf' stands for rotation free, so $\mathbf{v}^{k,\mathrm{df}}$ is the divergence free part of the optical flow vector field $\mathbf{v}^k$ at the kth time frame whereas for example $\mathbf{h}^{k,\mathrm{rf}}$ stand for the rotation free part of the gauge field $\mathbf{h}^k$ at the kth time frame.

Now since the perturbation $\boldsymbol{\delta}$ is arbitrary in a test-space dense in $\mathbf{L}_2(\Omega)$ the vector field in the left slot vanishes for the optimal vector field $\mathbf{v}^k$. This also means that its divergence free part and rotation free part vanishes[7] but at this point we must be careful $\mathbf{v}^k$ divergence free and $\mathbf{h}^k$ divergence free does not imply that the covariant derivative $D^{\mathbf{h}^k}\mathbf{v}^k$ is divergence free.

The next lemmas show how to proceed.

Lemma 9.2 *Let $\boldsymbol{a}$ and $\boldsymbol{b}$ be two smooth vector fields on $\Omega \subset \mathbb{R}^2$. Then we have $(D^{\boldsymbol{a}})^* D^{\boldsymbol{a}}\boldsymbol{b}) = -\Delta\boldsymbol{b} + Q^{\boldsymbol{a}}\boldsymbol{b}$, with $Q^{\boldsymbol{a}}\boldsymbol{b} = \sum_{j=1}^{2} \frac{\Delta a^j}{a^j} b^j \boldsymbol{e}_j$ with $\boldsymbol{e}_1 = (1,0)^T$ and $\boldsymbol{e}_2 = (0,1)^T$ in a cartesian coordinate frame.*

This result follows by direct computation.

Lemma 9.3 *Let $\boldsymbol{q}$ be a smooth vector field with compact support within Ω. If $(\boldsymbol{q}, \boldsymbol{\delta}^{df}) = 0$ for all divergence free perturbations $\boldsymbol{\delta}^{df}$ then $rot\,\boldsymbol{q} = 0$. If $(\boldsymbol{q}, \boldsymbol{\delta}^{rf}) = 0$ for all rotation free perturbations $\boldsymbol{\delta}^{rf}$ then $div\,\boldsymbol{q} = 0$. If $(\boldsymbol{q}, \boldsymbol{\delta}^{df}) = 0$ for all divergence free perturbations $\boldsymbol{\delta}^{d}$ then $\widetilde{rot}\,\boldsymbol{q} = 0$.*

[7] In case the vector field does not vanish at the boundary, one must subtract the harmonic infilling as in Eq. (5.23).

Proof follows directly from the Helmholtz decomposition (5.23) (the harmonic infilling vanishes) and integration by parts yields $\int_\Omega \widetilde{\text{rot}}\, A \cdot \nabla\phi \mathrm{d}\mathbf{x} = 0$.

From these lemmas we conclude that the Euler-Lagrange equations of (9.84) are given by

$$
\begin{array}{ll}
1. & \text{rot}\left(-\lambda(D^{\mathbf{h}^k,\text{df}})^* D^{\mathbf{h}^k,\text{df}}\mathbf{v}^{k,\text{df}} + \mathcal{S}_k\Lambda_k\mathcal{S}_k\mathbf{v}^{k,\text{df}}\right) = 0\ , \\
2. & \text{div}\left(-\lambda(D^{\mathbf{h}^k,\text{df}})^* D^{\mathbf{h}^k,\text{df}}\mathbf{v}^{k,\text{df}} + \mathcal{S}_k\Lambda_k\mathcal{S}_k\mathbf{v}^{k,\text{df}}\right) = \Delta\varphi\ , \\
3. & \text{rot}\left(-\lambda(D^{\mathbf{h}^k,\text{rf}})^* D^{\mathbf{h}^k,\text{rf}}\mathbf{v}^{k,\text{rf}} + \mathcal{S}_k\Lambda_k\mathcal{S}_k\mathbf{v}^{k,\text{rf}}\right) = 0\ , \\
4. & \text{rot}\left(-\lambda(D^{\mathbf{h}^k,\text{rf}})^* D^{\mathbf{h}^k,\text{rf}}\mathbf{v}^{k,\text{rf}} + \mathcal{S}_k\Lambda_k\mathcal{S}_k\mathbf{v}^{k,\text{rf}}\right) = -\Delta A\ , \\
5. & \text{rot}\left(\mathbf{v}^{k,\text{rf}}\right) = 0\ , \\
6. & \text{div}\left(\mathbf{v}^{k,\text{df}}\right) = 0\ , \\
7. & \text{rot}\left(\mathbf{h}^{k,\text{rf}}\right) = 0\ , \\
8. & \text{div}\left(\mathbf{h}^{k,\text{df}}\right) = 0\ ,
\end{array}
\tag{9.86}
$$

where φ and A are smooth scalar fields such that

$$
\begin{aligned}
&-\lambda(D^{\mathbf{h}^k,\text{df}})^* D^{\mathbf{h}^k,\text{df}}\mathbf{v}^{k,\text{df}} + \mathcal{S}_k\Lambda_k\mathcal{S}_k\mathbf{v}^{k,\text{df}} = \nabla\varphi\ , \\
&-\lambda(D^{\mathbf{h}^k,\text{rf}})^* D^{\mathbf{h}^k,\text{rf}}\mathbf{v}^{k,\text{rf}} + \mathcal{S}_k\Lambda_k\mathcal{S}_k\mathbf{v}^{k,\text{rf}} = \widetilde{\text{rot}}\, A.
\end{aligned}
$$

Note that

$$
\begin{aligned}
&\Delta\varphi = \text{div}\, Q^{\mathbf{h}^k,\text{df}}\mathbf{v}^{k,\text{df}}\ , \\
&-\Delta A = \widetilde{\text{rot}}\, Q^{\mathbf{h}^k,\text{rf}}\mathbf{v}^{k,\text{rf}}.
\end{aligned}
$$

Now in our algorithm depicted in Figure 1 we have set $\varphi = A =$ constant which means that we have dropped 5. and 6. in (9.86). To this end we note that the solutions of the remaining equations (under the assumption $\varphi = A =$ constant)

$$
\begin{aligned}
&\mathbf{v}^{k,\text{df}} := (-\lambda(D^{\mathbf{h}^k,\text{df}})^* D^{\mathbf{h}^k,\text{df}} + \mathcal{S}_k\Lambda_k\mathcal{S}_k)^{-1}\mathcal{S}_k^*\Lambda_k\mathbf{d}^{k,\text{df}}\ , \\
&\mathbf{v}^{k,\text{rf}} := (-\lambda(D^{\mathbf{h}^k,\text{rf}})^* D^{\mathbf{h}^k,\text{rf}} + \mathcal{S}_k\Lambda_k\mathcal{S}_k)^{-1}\mathcal{S}_k^*\Lambda_k\mathbf{d}^{k,\text{rf}}\ ,
\end{aligned}
$$

need not be divergence free and rotation free. However, in practice we have observed that they are respectively *nearly* divergence free and rotation free, since the relative error $\delta = \frac{\|V - V_{\text{rotfree/divfree}}\|}{\|V\|} << 10\%$.

10 Experiments

In order to assess accuracy of the proposed optic flow method depicted in Figure 1, we reconstruct/interpolate motion fields of two different phantoms from which we know the ground truth. Phantom one is a sequence consisting of 19 time-frames with size 99×99 pixels of purely contracting and expanding patterns (Figure 13 column 2), whereas phantom 2 consists of 13 frames of 93×93 pixels in size and displays non rigid rotation (13, column 4). Equations for phantom 1 have been provided in [5], whereas detailed description of phantom 2 has been carried out in [43]. Both phantoms vanish at the boundaries. Extraction of the motion field has been carried out at several spatial scales $s = \{1, 1.22, 1.48, 1.81, 2.21, 2.69, 3.28, 4.\}$ with time scale 1. In table 1 we display performance of the optic flow method, where the smoothness component has been described in terms of standard derivatives, covariant derivatives, and covariant derivatives combined with Helmholtz decomposition. In the assessment we employ the error measure based on the average angular error (AAE) [4],expressed in degrees, the L2 norm and their correspondent standard deviation. Algorithm evaluation has been performed on frame 5, 6 and 7 for phantom 1 and frame 3, 4 and 5 for phantom 2. We show that the proposed algorithm provides the most accurate reconstruction reaching $AAE = 0.97 \pm 0.62$ degrees and L2 norm error of $3.3 \times 10^{-2} \pm 0.03$ for phantom 1 and $AAE = 6.68 \pm 9.48$ degrees and L2 norm error of 0.16 ± 0.24 for phantom 2.

Since our approach consists of separate reconstruction of the divergence and rotation free part we index our parameters accordingly. For example λ_1 controls the degree of smoothness in the dense flow field

reconstruction of the rotation free part and η_2 denotes the interpolation parameter between covariant and standard derivatives of the dense flow field reconstruction of the divergence free part.

Increasing the value of $\lambda > 0$ increases the smoothness of the reconstructed motion field. We choose λ such that minimizes the AAE and L2 norm error of our phantoms with ground truth, where we set a range of values defined beforehand such as $\lambda = \{10^{-2}, 10^{-1}, 1, 10, 100, 10^3, 10^4, 10^5, 10^6\}$ and we normalize them with respect to the frame size. The reconstruction method based on conventional derivatives showed best results at $\lambda = 10^{-2}$ and $\lambda = 1$ for phantom 1 and phantom 2 respectively. The reconstruction method based on covariant derivative performed best at $\lambda = 10^2$ and $\lambda = 10$ for phantom 1 and phantom 2 respectively.

In case of reconstruction based on covariant derivatives and Helmholtz decomposition, we assign a fixed component $\lambda_2 = 10^2$ and $\lambda_1 = 10^2$ for phantom 1 and phantom 2 respectively and we choose the other λ component from the already defined range. In figure 14 we displayed the AAE behavior for phantom 1 and 2 using the proposed technique imposing different values to λ_1 for phantom 1 and to λ_2 for phantom 2. Here the horizontal axis is expressed in a logarithmic scale with base 10. Best performance are achieved at $\lambda_1 = 10^{-2}$ ($\log_{10} \lambda_1 = -5.99$) and at $\lambda_2 = 10^3$ ($\log_{10} \lambda_2 = 0.06$) for phantom 1 and phantom 2 respectively.

Once the choice of the λ_i parameter is established, we investigate parameter η_i, $i = 1, 2$ which takes into account the influence of the gauge field in the velocity field reconstruction, recall Subsection 7.2.1.

In the experiments we impose a gauge field equal to the outcome of optic flow method based on conventional derivatives (Figure 1). This is only one of the possible gauge field choices. Again we select parameter η from a range of a values $\eta = \{0.5, 0.7, 0.9, 1., 1.1, 1.3\}$ such that AAE is minimized. The reconstruction method based on covariant derivatives achieved best results for $\eta = 0.7$ and $\eta = 0.9$ for phantom 1 and 2 respectively. In case of the reconstruction method based on covariant derivative and Helmholtz decomposition we assign a fixed η, $\eta_2 = 0.5$ and $\eta_1 = 0.5$ for phantom 1 and 2 respectively, and we choose the other η_i from the defined range. In figure 15 we display the behavior of AAE for phantom 1 and 2 for different values of η. The proposed reconstruction method provides best performance for $\eta_1 = 0.9$ and $\eta_2 = 0.7$ for phantom 1 and 2 respectively.

	Error Measurements Phantom 1		Error Measurements Phantom 2	
Reconstruction Methodology	AAE	L2 Norm	AAE	L2 Norm
Conventional Derivatives	$1.26° \pm 1.11°$	$4.2 \times 10^{-2} \pm 0.04$	$8.05° \pm 9.09°$	0.21 ± 0.26
Covariant Derivatives	$1.20° \pm 1.01°$	$3.6 \times 10^{-2} \pm 0.03$	$7.30° \pm 9.81°$	0.19 ± 0.25
Helmholtz Dec. and Covariant Derivatives	$0.97° \pm 0.62°$	$3.3 \times 10^{-2} \pm 0.03$	$6.68° \pm 9.48°$	0.16 ± 0.24

Table 2: Performance of the proposed optic flow method using different reconstruction modalities. In the experiments the Average Angular Error (AAE), is expressed in degrees, L2 norm and their correspondent standard deviation have been employed as error measurement. Best performances are obtained by Helmholtz Decomposition and Covariant Derivative reconstruction method, $AAE = 0.97° \pm 0.62°$ and $L2 = 3.3 \times 10^{-2} \pm 0.03$ for phantom 1, and $AAE = 6.68° \pm 9.48°$ and $L2 = 0.16 \pm 0.24$ for phantom 2.

Divergence free and rotation free parts of the vector field may be employed to reveal and quantify abnormal deformation in the tissue. In the experiments we compare behavior of motion fields extracted from a healthy volunteer and from a patient, whose heart displays infarcted areas as indicated in Figure 16. Acquisition of heart images has been performed during systolic phase; we assess 11 frames with resolution of 86×86 pixels and pixel size of 1.2 *mm*. In figure 17 we respectively show the sampled motion field (column 1), rotation free (column 2) and divergence free (column 3) parts of frame 3,6 and 8 for the healthy heart case (row 1,2,3) and the diseased case (row 4,5,6) respectively. By means of our Helmholtz decomposition we observe that the healthy cardiac muscle starts to systole with intense rotation (row 1, column 3) and little contraction (row 1, column 2). At halfway the systolic phase, the contribution of rotation free parts becomes qualitative similar to the contribution of the divergence free part, that is, vectors inside the cardiac walls present similar absolute length (row 2, column 2 and 3). At the end of the systolic phase, contraction becomes more relevant (row 3, column 2), whereas rotation is almost absent (row 3, column 3). In the investigated diseased case, the heart exerts modest rotation through the whole sequence (row 4,5,6 and column 3), leaving contraction as the almost only contribution to the heart beat (row 4,5,6 and column 2).

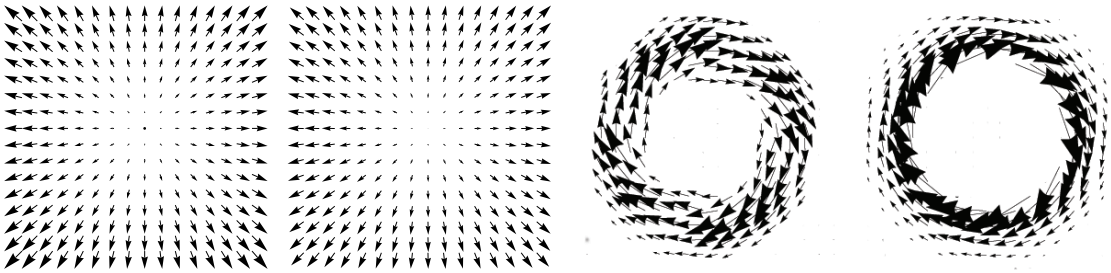

Figure 13: Phantoms and reconstructed vector fields. Column 1 and 2 display frame 5 of the expanding and contracting phantom: ground truth (column 1) and reconstructed vector field using the proposed algorithm (column 2). Column 3 and 4 display frame 3 of the rotating phantom: ground truth (column 3) and reconstructed vector field using the proposed algorithm (column 4).

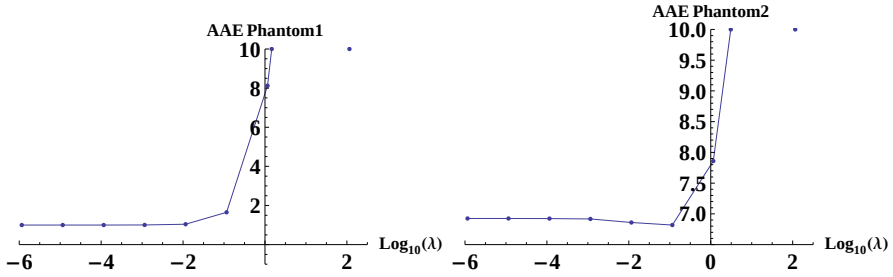

Figure 14: Performance of velocity field reconstruction method based on covariant derivatives and Helmholtz decomposition using different values for smoothing parameter λ (expressed in logarithmic scale). The experiments have been carried out with fixed $\lambda_2 = 10^2$ for phantom 1 and $\eta_1 = 10^2$ for phantom 2, and we vary parameter η_1 for phantom 1 and η_2 for phantom 2 according to a predefined range, such that $\lambda = \{10^{-2}, 10^{-1}, 1, 10, 100, 10^3, 10^4, 10^5, 10^6\}$. Left plot displays AAE behavior for phantom 1. Best performance $AAE = 0.97^\circ \pm 0.62^\circ$ for $\lambda_1 = 10^{-2}$ ($\log_{10} \lambda_1 = -5.99$). Right plot shows AAE behavior for phantom 2. Best results $AAE = 6.68^\circ \pm 9.48^\circ$ are achieved for $\lambda_2 = 10^3$ ($\log_{10} \lambda_2 = 0.06$).

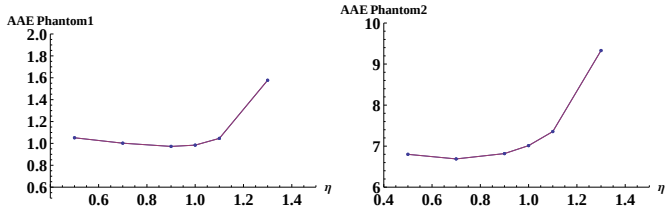

Figure 15: AAE behavior for different values of parameter η for the reconstruction method based on both covariant derivatives and Helmholtz decomposition. Parameter η takes into account influence of gauge field, recall Subsection 7.2.1. In the experiments we keep fixed $\eta_2 = 0.5$ for phantom 1 and $\eta_1 = 0.5$ for phantom 2, and we vary parameter η_1 for phantom 1 and η_2 for phantom 2 according to a predefined range $\eta = \{0.5, 0.7, 0.9, 1., 1.1, 1.3\}$. Left plot shows AAE behavior for phantom 1. Best performance $AAE = 0.97^\circ \pm 0.62^\circ$ is obtained for $\eta_1 = 0.9$. Right plot shows AAE behavior for phantom 2. Best results $AAE = 6.68^\circ \pm 9.48^\circ$ are achieved for $\eta_2 = 0.7$.

11 Discussion and Conclusion

In this paper we introduce an new approach to estimate cardiac motion by means of gauge fields and Helmholtz decomposition, and we provide a tool to explore the heart behavior.

The proposed optic flow technique contains regularization components described in terms of covariant

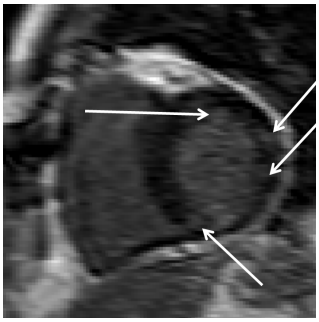

Figure 16: Diseased Heart. Arrows show areas where infarction occurred

derivatives, $\partial^{(h^j)}_{x^i} v^j = \frac{\partial v^j}{\partial x^i} - \frac{\frac{\partial h^j}{\partial x^i}}{h^j} v^j$, where $\mathbf{v} = (v^1, v^2)^T$ and $\mathbf{h} = (h^1, h^2)^T$ are respectively the unknown optical flow vector field and chosen gauge field. Gauge fields influence the regularization of the flow field reconstruction (see Section 6 and 8) and in the energy minimization process they typically put an a priori balance between magnitude and spatial variations of velocities. In this new approach the smoothness term does not penalize for changes from an imposed global assumption such as isotropic or anisotropic smoothness, like in many methods in the literature, but rather penalizes for deviations from a predefined motion model: in our case the gauge field.

We have shown that the covariant Laplacian is coercive and as result the Euler lagrange system of the minimization problem is well-posed. By expansion in B-splines we re-express the Euler Lagrange system in a discrete setting and we derive the stable solutions of this system numerically. Furthermore, we include a fast multi-scale Helmholtz decomposition with the aim to reconstruct the divergence free and rotation free parts of the vector field separately.

We have tested the method with two different phantoms and the extracted motion fields have been compared with the outcomes of similar techniques, for which the smoothness component was expressed in terms of conventional derivatives and covariant derivatives only. The proposed approach provided the best performance and shows the advantage of both using covariant derivatives and using Helmholtz decomposition. Besides improving the quality of reconstruction, Helmholtz decomposition is used as a tool to study cardiac behavior, since vector field decomposition allows to analyze cardiac contraction and cardiac rotation independently.

Finally, we have applied our method on real tagged MR images displaying the left ventricle of a healthy volunteer and a patient. Qualitative results illustrate the reliability of the estimated motion field.

Future work and further improvements

In the algorithm we use gauge fields obtained from outcomes of optic flow equations based on standard derivatives. This is just one of the possible choices. Gauge fields could also be deformed according to criteria that specifically reflect the heart behavior. Finally, the assessment has been carried out on 2 real data-sets. It would be interesting to apply the proposed technique on a larger population of images acquired from different volunteers and patients, with the aim to extract parameters that characterize cardiac healthy behavior from presence of diseases.

From the theoretical point of view we would like to investigate if it is possible to choose the Christoffel symbols (7.41) differently such that the Hilbert-Schmidt norm $|||D^{\mathbf{h}}\mathbf{v}|||$ of the covariant derivatives is invariant under rotation of both the unknown flow field $\mathbf{v}$ and the gauge field $\mathbf{h}$. Furthermore, we would like to derive an algorithm that solves the *single* Euler-Lagrange system explained in Subsection 9.1.

A Derivation Green's function of the 1D covariant Laplacian and related (in)equalities

In this section we derive the Green's function and prove equalities (7.56), (7.57), (7.58) and (7.59) and investigate how sharp the lower bound is if applied to Example 1 and Example 2.

Let $h \in C^2([0,1])$, $h > 0$ and Consider the following PDE system on $[0,1]$

$$(D^h)^* D^h f = \delta_y$$
$$\text{and } f \in \mathbb{H}_0^1([0,1]), \text{ i.e. } f \in \mathbb{H}_0^1([0,1]) \text{ and } f(0) = f(1) = 0.$$

This system has a unique solution, this follows by the the Riesz Theorem (or in particular Lax-Milgram Theorem). Recall that point evaluation $\psi \mapsto \delta_y(\psi) = \psi(y)$ is a continuous linear functional on $\mathbb{H}_0^1([0,1])$ and the left hand side is a bounded, coercive sesquilinear form on $\mathbb{H}_0^1([0,1])$ due to the compact embedding of $\mathbb{H}_0^1([0,1])$ into $\mathbb{L}_2([0,1])$.

Now we set $\phi = D^h f \in \mathbb{L}_2([0,1])$ then $(D^h)^*\phi = 0$ implies that $-\phi' - \frac{h'}{h}\phi = 0$. this is equivalent to

$$\phi\, h' + \phi'\, h = 0 \Leftrightarrow h(x)\phi(x) = c_1$$

for every $x \in [0,1]$ and some constant $c_1 > 0$. The substitution $\phi(x) = f'(x) - \frac{h'(x)}{h(x)} f(x)$ yields

$$f'(x)h(x) - h'(x)f(x) = c_1 \ .$$

This first order ODE has as homogeneous solution $f = c_2 h$ and by variation of constants formula we find the standard solutions

$$f(x) = c_2 h(x) + c_1\, h(x)\, Q(x), \text{ with } Q_h(x) := \int_0^x h(v)^{-2} \mathrm{d}v \ .$$

Now within this class we find solutions f_0 and f_1 with $f_0(0) = 0$, $f_0(1) = 1$, $f_1(0) = 1$ and $f_1(1) = 0$ such that

$$f_0(x) = h(x)Q_h(x) \text{ and } f_1(x) = h(x)(Q_h(1) - Q_h(x)) \ ,$$

The (constant) Wronskian of these solutions equals $W = f_0'(0)f_1(0) - f_0(0)f_1'(0) = \frac{1}{Q_h(1)h(1)h(0)}$. Now the kernel operator K_h given by (7.56) or equivalently

$$(K_h f)(x) = \frac{1}{W} \begin{cases} f_0(x)f_1(y) & x \le y, \\ f_0(y)f_1(x) & x > y, \end{cases} = \frac{1}{W} \left(f_1(x) \int_0^x f_0(y)f(y)\,\mathrm{d}y + f_0(x) \int_x^1 f_0(y)f(y)\,\mathrm{d}y \right)$$

is the right inverse of the operator $(D^h)^* D^h$, where we note that $K_h f \in \mathbb{H}_0^2([0,1])$ and

$$(D^h)^* D^h K_h f = f \ .$$

This equality can be straightforwardly verified where we note

$$Kf''(x) = \frac{1}{W} \left(f_1''(x) \int_0^x f_0(y)f(y)\mathrm{d}y - f_0''(x) \int_x^1 f_1(y)f(y)\mathrm{d}y - W f(x) \right),$$

so that indeed $-(Kf)'' + \frac{h''}{h} K_h f = f$.

Regarding (7.59) we note that $k_h(x,y) = k_h(y,x)$ and

$$\begin{aligned} \|K_h\|^2 &\le |||K_h|||^2 = \mathrm{trace}\{K_h^* K_h\} = \|k_h\|^2_{\mathbb{L}_2([0,1]\times[0,1])} \\ &\le \tfrac{2}{(Q_h(1))^2} \int_0^1 \int_0^y h^2(x)h^2(y)Q_h^2(x)(Q_h(1) - Q_h(y))^2 \mathrm{d}x\mathrm{d}y \\ &= \tfrac{2}{(Q_h(1))^2} \int_0^1 h^2(y)(Q_h(1) - Q_h(y))^2 \left(\int_0^y h^2(x)Q^2(x)\mathrm{d}x \right) \mathrm{d}y \\ &\le 2(Q_h(1))^2 \|h\|^4_{\mathbb{L}_2([0,1])} = 2 \left(\int_0^1 h^{-2}(y)\mathrm{d}y \right)^2 \left(\int_0^1 h^2(y)\mathrm{d}y \right)^2 , \end{aligned}$$

where we used that $0 \leq Q(x) \leq Q(1)$.

Finally, we note the following result (which can also be observed in Figure 11).

Lemma A.4 *if the gauge function $h > 0$ is convex (respectively concave) then the corresponding Green's function $k(\cdot, y) = ((D^h)^*)D^h)^{-1}\delta_y$ of the covariant Laplacian is convex (respectively concave) as well.*

Proof This follows from the fact that both f_0 and f_1 and their Wronskian are positive (due to $0 \leq Q(x) \leq Q(1)$), so for example suppose $x \leq y$ then $\frac{\partial^2}{\partial x^2} k_h(x,y) = W^{-1} f_0''(x) f_1(y) = +\frac{h''(x)}{h(x)}(W^{-1} f_0(x) f_1(x))$ □

References

[1] Arfken, G.B., Weber, H.J.: Mathematical Methods for Physicists. Academic Press, San Diego (1995)

[2] van Assen, H.C., Florack, L.M.J., Suinesiaputra, A., Westenberg, J.J.M., ter Haar Romeny, B.M.: Purely evidence based multi-scale cardiac tracking using optic flow. In: MICCAI 2007 workshop on CBM II, pp. 84–93 (2007)

[3] Axel, L., Dougherty, L.: MR imaging of motion with spatial modulation of magnetization. Radiology **171**(3), 841–845 (1989)

[4] Barron, J.L., Fleet, D.J., Beauchemin, S.: Performance of optical flow techniques. IJCV **12**(1), 43–77 (1994)

[5] Becciu, A., Janssen, B.J., Assen, H., Florack, L., Roode, V., Haar Romeny, B.M.: Extraction of cardiac motion using scale-space features points and gauged reconstruction. In: CAIP '09: Proceedings of the 13th International Conference on Computer Analysis of Images and Patterns, pp. 598–605. Springer-Verlag, Berlin, Heidelberg (2009)

[6] Bruhn, A., Weickert, J., Kohlber, T., Schnoerr, C.: A multigrid platform for real-time motion computation with discontinuity-preserving variational methods. IJCV **70**(3), 257–277 (2006)

[7] Corpetti, T., Memin, E., Perez, P.: Dense estimation of fluid flows **24**(3), 365–380 (2002)

[8] Dorst, P., Janssen, B., Florack, L., ter Haar Romeny, B.: Optic flow using multi-scale anchor points. In: Proceedings of The 13th International Conference on Computer Analysis of Images and Patterns (CAIP09), Lecture Notes in Computer Science. Springer Verlag, Berlin (2009)

[9] Duits, R.: Perceptual organization in image analysis. Ph.D. thesis, Eindhoven University of Technology, Department of Biomedical Engineering, The Netherlands (2005). A digital version is available on the web: URL: http:// www.bmi2.bmt.tue.nl/Image-Analysis/People/RDuits/THESISRDUITS.pdf

[10] F. Sheehan and D. Stewart and H. Dodge and S. Mitten and E. Bolson and and G. Brown: Variability in the measurement of regional left ventricular wall motion. Circulation **68**, 550–559 (1983)

[11] Florack, L., Kuijper, A.: The topological structure of scale-space images. Journal of Mathematical Imaging and Vision **12**(1), 65–79 (2000)

[12] Florack, L.M.J.: Image Structure. Computational Imaging and Vision. Kluwer Academic Publishers, Dordrecht, The Netherlands (1997)

[13] Florack, L.M.J., van Assen, H.C.: Dense multiscale motion extraction from cardiac cine MR tagging using HARP technology. In: ICCV workshop on MMBIA (2007)

[14] Florack, L.M.J., Niessen, W., Nielsen, M.: The intrinsic structure of optic flow incorporating measurements of duality. IJCV **27**(3), 263–286 (1998)

[15] Forssen, P.: Low and medium level vision using channel representations. Ph.D. thesis, Linkoping University, Dept. EE, Linkoping, Sweden (2004)

[16] Gabor, D.: Theory of communication. J. IEE **93**(26), 429–457 (1946)

[17] Georgiev, T.: Relighting, retinex theory, and perceived gradients. In: Proceedings of Mirage 2005, INRIA Rocquencourt (2005)

[18] Gerschgorin, S.: Ueber die abgrenzung der eigenwerte einer matrix. Izv. Akad. Nauk. USSR Otd. Fiz.-Mat. Nauk. **7**, 550–559 (1931)

[19] Groetsch, C.: Elements of Applicable Functional Analysis. Marcel Dekker Inc., New York, Basel (1980)

[20] Gupta, S., Gupta, E.N., Prince, J.L.: Stochastic models for div-curl optical flow methods. IEEE Signal Processing Letters **3**, 32–35 (1996)

[21] ter Haar Romeny, B.M.: Front-End Vision and Multi- Scale Image Analysis: Multiscale Computer Vision Theory and Applications, written in Mathematica. Computational Imaging and Vision. Kluwer Academic Publishers, Dordrecht, The Netherlands (2003)

[22] Hansen, P.C., Nagy, J.G., O'Leary, D.P.: Deblurring Images: Matrices, Spectra, and Filtering, 1 edn. SIAM (2006)

[23] von Helmholtz, H.: Ueber integrale der hydrodynamischen gleichungen, welche den wirbelbewegungen entsprechen. Crelles J. **55**(25) (1858)

[24] Horgan, C.O., Nemat-Nasser, S.: Bounds on eigenvalues of sturm-liouville problems with discontinuous coefficients. Journal of Applied Mathematics and Physics **30**, 77–86 (1979)

[25] Horn, B.K.P., Shunck, B.G.: Determining optical flow. AI **17**, 185–203 (1981)

[26] Iijima, T.: Basic theory on normalization of a pattern (in case of typical one-dimensional pattern). Bulletin of Electrical Laboratory **26**, 368–388 (1962). (in Japanese)

[27] Janssen, B.: Representation and manipulation of images based on linear functionals. Ph.D. thesis, Eindhoven University of Technology, Eindhoven, The Netherlands (2009). URL: http://alexandria.tue.nl/extra2/200911295.pdf

[28] Janssen, B., Duits, R.: Linear image reconstruction by sobolev norms on the bounded domain. International Journal of Computer Vision. **84**(2), 205–219 (2009)

[29] Janssen, B., Florack, L., Duits, R., ter Haar Romeny, B.: Optic flow from multi-scale dynamic anchor point attributes. In: A. Campilho, M. Kamel (eds.) Image Analysis and Recognition, Third International Conference, ICIAR 2006, *Lecture Notes in Computer Science*, vol. 4141, pp. 767–779. Springer Verlag, Berlin (2006)

[30] Janssen, B.J., Duits, R., Florack, L.M.J.: Coarse-to-fine image reconstruction based on weighted differential features and background gauge fields. LNCS **5567**, 377–388 (2009)

[31] Koenderink, J.J.: The structure of images. Biol. Cybern. **50**, 363–370 (1984)

[32] Kohlberger, T., Memin, E., Schnorr, C.: Variational dense motion estimation using the helmholtz decomposition. pp. 432–448 (2003)

[33] Kuijper, A.: The deep structure of gaussian scale space images. Ph.D. thesis, University of Utrecht (2002)

[34] Lindeberg, T.: Scale-space for discrete signals **12**(3), 234–245 (1990)

[35] Lindeberg, T.: Scale-Space Theory in Computer Vision. The Kluwer International Series in Engineering and Computer Science. Dordrecht, The Netherlands (1994)

[36] Lindeberg, T.: Scale-Space Theory in Computer Vision. First edn. The Springer Intern. Series in Engineering and Computer Science. Kluwer Academic Publishers, Dordrecht, The Netherlands (1994)

[37] Milgram, P.D. and Lax, A. N.: Parabolic equations. Contributions to the theory of partial differential equations, Annals of Math. Studies **30**, 167–190 (1954)

[38] Niessen, W., Duncan, J., Nielsen, M.L.F., ter Haar Romeny, B., Viergever, M.: A multiscale approach to image sequence analysis. Computer Vision and Image Understanding **65**(2), 259–268 (1997)

[39] Nir, T., Bruckstein, A., Kimmel, R.: Over-Parameterized variational optical flow. International Journal of Computer Vision **76**(2), 205–216 (2008)

[40] Osman, N.F., McVeigh, W.S., Prince, J.L.: Cardiac motion tracking using cine harmonic phase (harp) magnetic resonance imaging. Magnetic Resonance in Medicine **42**(6), 1048–1060 (1999)

[41] Platel, B.: Exploring the deep structure of images. Ph.D. thesis, Eindhoven University of Technology (2007)

[42] Rudin, W.: Functional Analysis. McGraw-Hill, New York (1973)

[43] Simonis, F.F.J.: Optical flow analysis on a deforming phantom. Tech. rep. (2009)

[44] Staal, J., Kalitzin, S., ter Haar Romeny, B.M., Viergever, M.: Detection of critical structures in scale space. In: Lecture Notes in Computer Science, vol. 1682, pp. 105–116 (1999)

[45] Suinesiaputra, A., Florack, L., Westenberg, J., ter Haar Romeny, B., Reiber, J., Lelieveldt, B.: Optic flow computation from cardiac MR tagging using a multiscale differential method a comparative study with velocity encoded MRI. In: Proceedings of MICCAI 2003, LNCS, Berlin, Springer-Verlag, pp. 483–490 (2003)

[46] Thirion, J.P.: Image matching as a diffusion process: an analogy with Maxwells demons. Medical Image Analysis **2**(3), 243–260 (1998)

[47] Tong, Y., Lombeyda, S., Hivani, A.N., Desbrun, M.: Discrete multiscale vector field decomposition. ACM Transactions on Graphics (TOG) **22**, 445–452 (2003)

[48] Unser, M.: Splines: A perfect fit for signal and image processing. IEEE Signal Processing Magazine **16**(6), 22–38 (1999)

[49] Weickert, J.A., Ishikawa, S., Imiya, A.: On the history of Gaussian scale-space axiomatics. In: Gaussian Scale-Space Theory, Computational Imaging and Vision Series, chap. 4, pp. 45–59. Kluwer Academic Publisher (1997)

[50] Wloka, J.: Partial Differential Equations. Cambridge University Press, Cambridge (1987)

[51] Zerhouni, E.A., Parish, D.M., Rogers, W.J., Yang, A., Sapiro, E.P.: Human heart: Tagging with MR imaging a method for noninvasive assessment of myocardial motion. Radiology **169**(1), 59–63 (1988)

[52] Zimmer, H., Bruhn, A., Weickert, J., Valgaerts, L., Salgado, A., Rosenhahn, B., Seidel, H.: Complementary optic flow. In: Proceedings of Energy Minimization Methods in Computer Vision and Pattern Recognition (EMMCVPR), LNCS, Berlin, Springer-Verlag, vol. 5681, pp. 207–220 (2009)

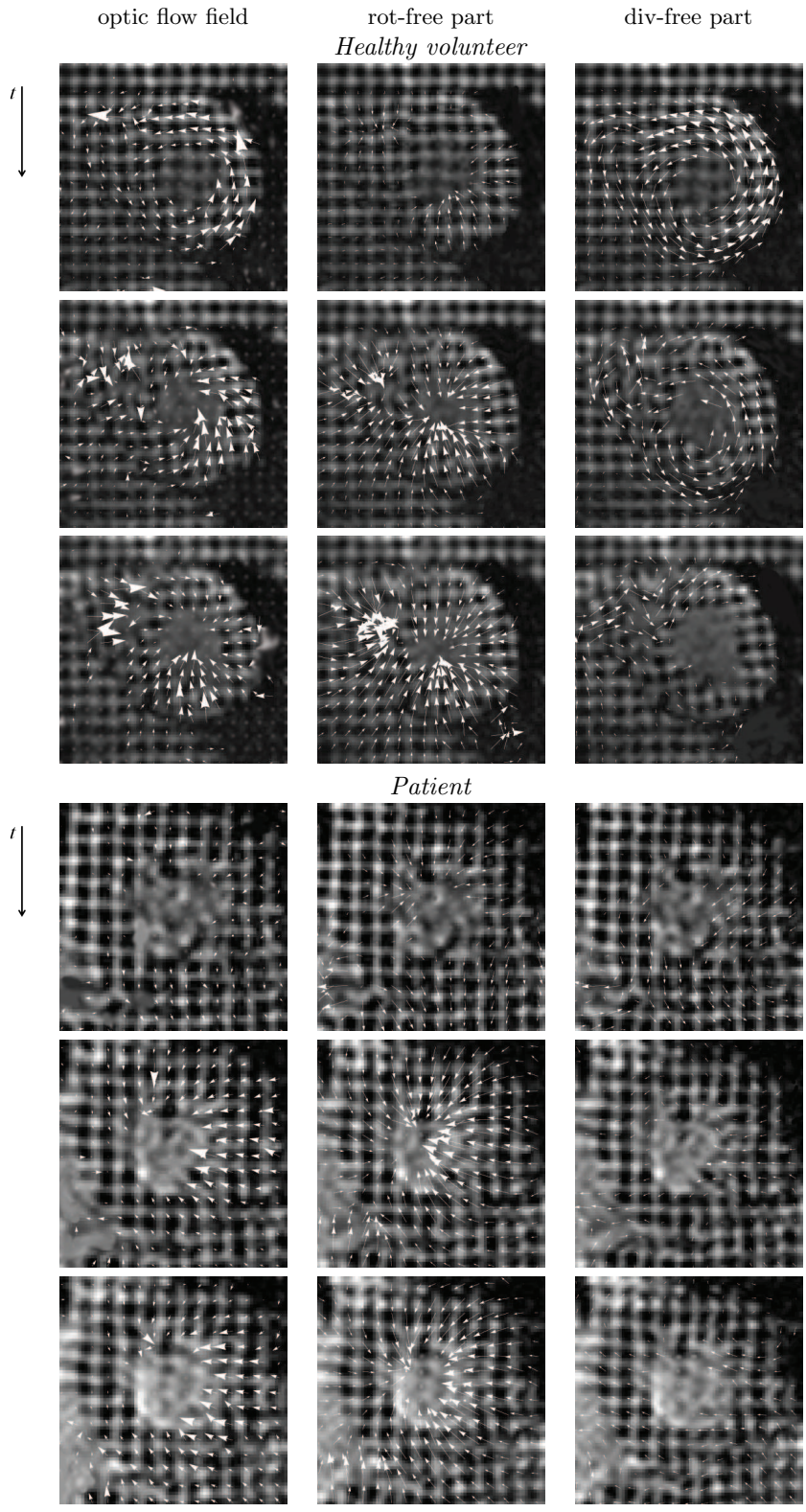

Figure 17: Cardiac motion field behavior for a healthy volunteer and a patient. We assess frame 3, 6 and 8 (row 1,2 and 3 healthy volunteer, row 4,5 and 6 patient) of a sequence of 11 frames displaying the cardiac muscle in phase of systole. Column 1 shows the extracted motion fields, column 2 shows the rotation free part, whereas column 3 shows the divergent free part.

PREVIOUS PUBLICATIONS IN THIS SERIES:

Number	Author(s)	Title	Month
10-27	N. Sepasian A. Vilanova J.H.M. ten Thije Boonkkamp B.M. ten Haar Romeny	An innovative geodesic based multi-valued fiber-tracking algorithm for diffusion tensor imaging	May '10
10-28	M.E. Hochstenbach L. Reichel	Subspace-restricted singular value decompositions for linear discrete ill-posed problems	May '10
10-29	M.E. Hochstenbach	Fields of values and inclusion regions for matrix pencils	May '10
10-30	A. Demir S.W. Rienstra	Sound radiation from a lined exhaust duct with lined afterbody	June '10
10-31	R. Duits A. Becciu B.J. Janssen L.M.J. Florack H. van Assen B. ter Haar Romeny	Cardiac motion estimation using covariant derivatives and Helmholtz decomposition	June '10

Ontwerp: de Tantes,
Tobias Baanders, CWI